The Pristine survey - V. A bright star sample observed with SOPHIE

P. Bonifacio, Elisabetta Caffau, F. Sestito, C. Lardo, Nicolas Martin, E. Starkenburg, L. Sbordone, P. François, P. Jablonka, A. A. Henden, et al.

MNRAS **000**, 1–21 (2019) Preprint 15 May 2019 Compiled using MNRAS LATEX style file v3.0

The Pristine survey - V. A bright star sample observed with SOPHIE ⋆

P. Bonifacio,[1] E. Caffau,[1] F. Sestito,[2,3] C. Lardo,[4] N. Martin,[2,5] E. Starkenburg,[3] L. Sbordone,[6] P. François [1], P. Jablonka,[1,4] A. A. Henden,[7] S. Salvadori,[8,9,1] J.I. González Hernández,[10] D. Aguado,[11] V. Hill,[12] K. Venn,[13] J. F. Navarro, A. Arentsen,[3] R. Sanchez-Janssen,[14] R. Carlberg[15]

[1] *GEPI, Observatoire de Paris, Université PSL, CNRS, Place Jules Janssen, 92195 Meudon, France*
[2] *Université de Strasbourg, CNRS, Observatoire astronomique de Strasbourg, UMR 7550, F-67000, France*
[3] *Leibniz-Institut für Astrophysik Potsdam (AIP), An der Sternwarte 16, 14482 Potsdam, Germany*
[4] *Laboratoire d'Astrophysique, Ecole Polytechnique Fédérale de Lausanne (EPFL), Observatoire de Sauverny, CH-1290 Versoix, Switzerland*
[5] *Max-Planck-Institut für Astronomie, Königstuhl 17, D-69117, Heidelberg, Germany*
[6] *European Southern Observatory, Alonso de Cordova 3109, Vitacura, Santiago, Chile*
[7] *AAVSO, Cambridge, Massachusetts, USA*
[8] *Dipartimento di Fisica e Astronomia, Universitá degli Studi di Firenze, Via G. Sansone 1, I-50019 Sesto Fiorentino, Italy*
[9] *INAF/Osservatorio Astrofisico di Arcetri, Largo E. Fermi 5, I-50125 Firenze, Italy*
[10] *Instituto de Astrofísica de Canarias, Vía Láctea, 38205, La Laguna, Tenerife*
[11] *Institute of Astronomy, University of Cambridge, Madingley Road, CB3 0HA Cambridge, UK*
[12] *Université Côte d'Azur, Observatoire de la Côte d'Azur, CNRS, Laboratoire Lagrange, Bd de l'Observatoire, CS 34229, 06304 Nice cedex 4, France*
[13] *Department of Physics and Astronomy, University of Victoria, PO Box 3055, STN CSC, Victoria BC V8W 3P6, Canada*
[14] *STFC UK Astronomy Technology Centre, The Royal Observatory Edinburgh, Blackford Hill, Edinburgh, EH9 3HJ, UK*
[15] *Department of Astronomy & Astrophysics, University of Toronto, Toronto, ON M5S 3H4, Canada*

Accepted XXX. Received YYY; in original form ZZZ

ABSTRACT

With the aim of probing the properties of the bright end of the Pristine survey and its effectiveness in selecting metal-poor stars, we selected a sample of bright candidate metal-poor stars combining Pristine $CaHK$ photometry with APASS gi photometry, before the Gaia second data release became available. These stars were observed with the SOPHIE spectrograph at the 1.93 m telescope of Observatoire de Haute Provence and we used photometry and parallaxes from Gaia DR2 to derive their atmospheric parameters. Chemical abundances were determined from the spectra for 40 stars of the sample. Eight stars were confirmed to be very metal-poor ([Fe/H]< -2.0), as expected from the photometric estimate. No star was found with [Fe/H]< -3.0 although for nine stars the photometric estimate was below this value. Three multiple systems are identified from their multi-peaked cross-correlation functions. Two metal-poor stars with [Fe/H]≈ -1.0 have an age estimate of about 4 Gyr. Accretion from a satellite galaxy is a possible explanation for these "young metal-poor stars", but they could also be field blue stragglers. Galactic orbits for our sample of stars allowed us to divide them into three classes that we label "Halo","Thick" and "Thin" and tentatively identify as halo, thick disc and thin disc. We present a new method for deriving photometric metallicities, effective temperatures and surface gravities by combining Gaia parallaxes, photometry and Pristine $CaHK$ photometry. Comparison with spectroscopic metallicities shows a very good agreement and suggests that we can further improve the efficiency of Pristine $CaHK$ in selecting metal-poor stars.

Key words: Stars: abundances – Stars: atmospheres – Stars: Population II – Stars: kinematics and dynamics – Galaxy: abundances – Galaxy: evolution

⋆ Based on observations acquired at the Observatoire de Haute Provence, programmes 17B.PNCG.BONI and 18A.PNCG.BONI.

1 INTRODUCTION

Very old stars are witnesses of the early phases of galaxy evolution, for this reason it is useful to study in detail large samples of such stars. Ever since Baade (1944) introduced the concept of Pop I and Pop II stars, it was clear that Pop II stars were rare objects characterised by high radial velocities (Oort 1926a,b) and peculiar spectra, with strong CH bands and weak CN bands (Lindblad 1922; Keenan 1942; Popper 1947; Keenan et al. 1948). It was not until the work of Schwarzschild et al. (1951) that it was clear that the weakening of the CN bands and strengthening of the CH bands can be ascribed to a lower abundance of metals in these stars. The same year Chamberlain & Aller (1951) demonstrated that the "A-type subdwarfs" HD 140283 and HD 119445 are deficient in Ca and Fe with respect ot the Sun.

In the following years the main source of metal-poor stars were objective prism surveys (Bidelman & MacConnell 1973; Bond 1980). Follow-up, observations then relied on suitable intermediate-band photometric observations (e.g. Norris et al. 1985, for DDO photometry) and, when possible on high-resolution spectroscopy (e.g. Luck & Bond 1981). At the end of the XX century two large scale objective-prism survey boosted considerably the number of known metal-poor stars: the HK Survey (Beers et al. 1985, 1992) and the Hamburg-ESO survey (Christlieb 2003). Some attempts were made for a follow-up to determine photometric metallicities for the HK survey (Anthony-Twarog et al. 2000) using the the $uvbyCa$ system (Anthony-Twarog et al. 1991; Twarog & Anthony-Twarog 1995; Anthony-Twarog & Twarog 1998), and using the $uvby-\beta$ system (Schuster et al. 1996, 1999, 2004). However this proved as time-consuming as medium resolution spectroscopy (e.g. Allende Prieto et al. 2000) and was not continued. Only in the XXI century, with the advent of wide-field CCD imagers, two surveys attempted to select metal-poor stars directly from photometry: the SkyMapper Southern Sky Survey (Keller et al. 2007; Casagrande et al. 2019) and the Pristine survey (Starkenburg et al. 2017, hereafter Paper I). Some attempts to select metal-poor stars have also been made using existing data-bases of spectral types (Meléndez et al. 2016) or wide-band surveys (Schlaufman & Casey 2014). For the latter catalogue the success rate is of the order of 3% for stars with [Fe/H]≤ -3.0 and 36% for stars with [Fe/H]≤ -2.0 (Schlaufman & Casey 2014; Placco et al. 2019). Two extremely metal poor stars selected from mismatch of the spectral-type with the colours and follow-up medium resolution spectroscopy have been published so far (Meléndez et al. 2016; Cain et al. 2018).

The Pristine Survey has proven to be successful in selecting extremely metal-poor stars at faint magnitudes, but has, so-far, not been as successful in selecting bright stars. This in spite of the fact that the $CaHK$ filter is so narrow that even stars with $V = 10$ are not saturated. In this paper we continue the investigation of bright candidate metal-poor stars in the Pristine Survey, that we began in Caffau et al. (2017, hereafter Paper II). In Paper II for the photometric selection we combined the Pristine $CaHK$ photometry with the broad band SDSS photometry (York et al. 2000). We concluded that at the bright end the SDSS photometry is not reliable because of saturation and we advocated the use of APASS (Henden et al. 2018, 2015; Henden & Munari 2014; Henden et al. 2009, https://www.aavso.org/apass) photometry instead. This survey is all-sky and has been designed precisely to bridge the magnitude gap between the all-sky photometry provided by the Tycho experiment on board the ESA Hipparcos satellite (Hoeg et al. 1997), with a limiting magnitude of V$\sim$ 11.5, and the large deep photometric surveys, like SDSS (York et al. 2000), that have a bright limit of $g \sim 14.5$. The sample presented in this paper has been in fact selected using Pristine $CaHK$ photometry and APASS photometry. We selected a sample of 47 stars, brighter than $g = 14.5$, and with estimated photometric metallicity below –1.5. The mean of the metallicities estimated from photometry is –2.51, nine stars were expected to have metallicity ≤ -3.0. We observed them at Observatoire de Haute Provence with the SOPHIE (Bouchy & Sophie Team 2006) spectrograph, fed by the 1.93 m telescope. To determine atmospheric parameters and orbits for our program stars we made use of the second data release (Gaia Collaboration et al. 2018; Arenou et al. 2018a, hereafter Gaia DR2) of the Gaia mission (Gaia Collaboration et al. 2016).

2 OBSERVATIONS AND DATA REDUCTION

The SOPHIE spectra were acquired during two runs, the first between February 16th and February 20th 2018 (observer P. Bonifacio) and the second between April 13th and April 17th 2018 (observer F. Sestito). We always used the High Efficiency mode, that provides a resolving power $R = 39\,000$, with one fibre on the object (fibre A) and one on the sky (fibre B). The spectra cover the wavelength range 387.2 nm to 694.3 nm. The typical integration time was 1h for each star. During the observations we aimed at a signal-noise-ratio, as estimated from the exposure-meter, in the range 15 to 20. For some stars we took several exposures or lengthened the exposure time in order to reach this.

The spectra were processed on the fly by the SOPHIE pipeline that makes use of the calibration frames taken at the beginning of the night (bias, flat-field, Th-Ar and Fabry-Perot étalon). The pipeline also does a cross-correlation analysis to determine the star's radial velocity v_r. We used the G2 or the K5 mask, depending on the star's effective temperature, for this cross-correlation. In spite of the low S/N ratio of the spectra, the formal error on the radial velocity estimated by the pipeline was of the order of a few tens of $\mathrm{m\,s^{-1}}$ and always less than $0.1\,\mathrm{km\,s^{-1}}$. The masks used are optimized for solar metallicity stars and some of our stars are definitively of lower metallicity. We measured some of the stars with our own software, using more appropriate masks, (see Sect. 3) and we concluded that the radial velocities measured by the SOPHIE pipeline are accurate, although a more appropriate estimate on the error in the radial velocity, including the template mismatch, is $0.5\,\mathrm{km\,s^{-1}}$. In order to make the spectra ready for analysis with MyGIsFOS (Sbordone et al. 2014), we subtracted the sky from the spectrum in fibre A and doppler shifted the spectrum by $-v_r$. To perform the sky subtraction we did not simply subtract the spectrum of fibre B from that of fibre A, since this would have severely degraded the signal-to-noise ratio. Instead we performed a median filtering of the sky spectrum prior to subtraction, and subtracted a mean sky continuum.

Table 1. Measured radial velocities of Pristine_113.6058+45.8841

BJD	RV1 km s^{-1}	RV2 km s^{-1}	Mean km s^{-1}	Comment
2458167.4587807	8.2	25.4	16.8	double peak
2458168.3459378	9.2	24.4	16.8	double peak
2458170.2661661			16.6	single peak
2458224.3983226			16.6	single peak
2458226.3199328			16.7	single peak

The drawback is that sky lines (both emission and absorption), cannot be subtracted. We therefore made sure not to use the spectral intervals affected by sky lines. In some cases, when the spectra were particularly noisy, we approximated the sky continuum by a spline fitted to a few continuum points selected interactively.

3 MULTIPLE SYSTEMS

Three stars in our sample showed multiple peaks in the cross-correlation function. Only one was observed at different epochs and for this system we can confirm that it is indeed a binary. For the other two stars we cannot exclude the presence of an alignment of unbound stars along the line of sight, although in no case suitable neighbouring stars were found in the Gaia DR2 data. Since the SOPHIE pipeline is not designed to extract radial velocities for stars with multiple peaks in the cross-corelation function, the radial velocities were determined for all three stars by cross-correlation over the range 420 nm – 680 nm. We used a synthetic spectrum, with parameters close to the photometric estimates of each star and the velocities were then measured by fitting gaussians to the peaks. The derived velocity is sensitive to the limits selected to perform the fit, repeated measurements allowed us to estimate an error of 0.3
kmskm s^{-1} [1]. For these stars we do not provide atmospheric parameters or chemical abundances. To estimate the effect of the veiling some hypothesis on the luminosity ratio of the two stars should be made. A reliable estimate can only be made if the orbital parameters of the binary are known.

3.1 Pristine_111.9501+44.1449

This system was observed only on the night of February 18th 2018, barycentric julian date BJD=2458168.2918411. The cross correlation function shown in Fig. 1 shows three distinct peaks at –102.4 km s^{-1}, –61.4 km s^{-1}and +67.6 km s^{-1}. In Gaia DR2 there is no nearby companion. Although we cannot exclude the possibility of a chance alignement we consider this unlikely. In order to produce a composite spectrum with lines from each star, the stars must be of roughly the same luminosity. If the three stars were not at the same distance, this would only be possible if they were in different evolutionary stages, hence different intrinsic luminosity, in a way to exactly compensate the difference in distance. Although not impossible, this seems contrived and it is more likely that this is a triple system. If so it must be hierarchical in order to be stable, thus there will be two stars of the triplet that are closer and a third one that orbits the couple. With a magnitude $G = 13.4$ this system will also have precise epoch radial velocities from the Gaia RVS. Nevertheless further observations of this system are strongly encouraged in order to allow to determine its orbit.

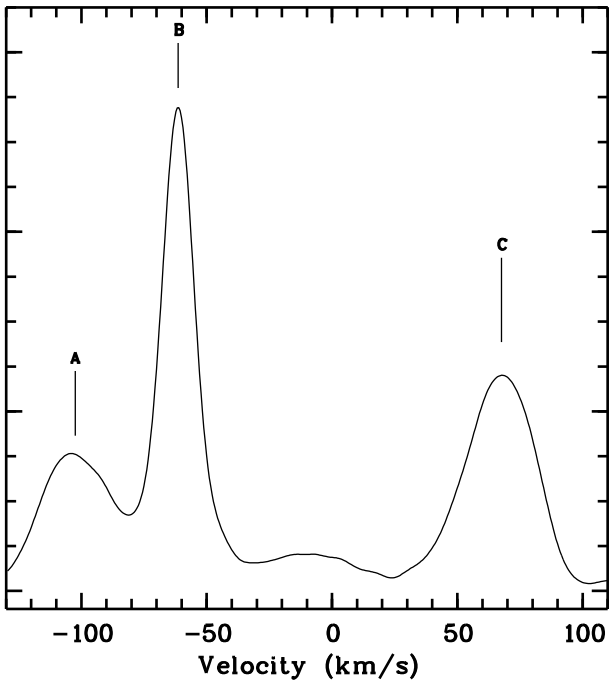

Figure 1. Cross correlation functions for Pristine_111.9501+44.1449 for the observation of February 18th 2018. Three peaks are clearly visible, marked A, B and C.

3.2 Pristine_113.6058+45.8841

This system was observed on three nights in February 2018 and on two nights in April 2018. On the night February 17th the cross-correlation function appears clearly double-peaked allowing for a clean determination of the radial velocities. The night after the cross-correlation function appeared again double peaked and the peaks moved closer by about 2 km s^{-1}. At the other three epochs the cross-correlation function appears single peaked, although broad. At these epochs it is impossible to determine reliably the radial velocities of the two components, we estimated the mean velocity of the system by fitting a single gaussian to the peak. The distortion of the line profiles suggests that in April the two systems "crossed", i.e. the system that appeared to the blue in February appears to the red in April. Given this system is bright ($G = 12.4$) the Gaia mission will provide accurate epoch radial velocities that will provide a reliable spectroscopic orbit.

[1] The estimated error here is smaller than what we estimated for the radial velocities measured by the SOPHIE pipeline, because in that case we estimated the error due to the template mismatch. In the case of the SOPHIE pipeline we could use only two templates for all the stars. Here the template has been selected carefully from a large library of synthetic spectra, to match closely the estimated parameters of each star.

Table 2. Stellar Parameters.

Star	RA[a] hms	DEC[a] dms	V mag	RV km s^{-1}	T$_{\rm eff}$ 10^3 K	log g [cgs]	ξ km/s	[Fe/H]
Pristine_110.0459+43.0522	07:20:11.03	+43:03:08	13.47	−84.9	5260	2.62	1.5	−2.42 ± 0.24
Pristine_110.4208+40.8947	07:21:41.01	+40:53:41	14.49	−85.5	5643	3.60	1.5	−1.57 ± 0.40
Pristine_111.5919+44.0179	07:26:22.07	+44:01:05	13.09	−51.4	6166	3.80	1.5	−0.70 ± 0.20
Pristine_112.0456+43.9914	07:28:10.90	+43:59:29	14.07	+15.3	6370	4.00	1.5	−0.53 ± 0.24
Pristine_112.3237+44.2279	07:29:17.70	+44:13:40	12.88	−0.9	6319	4.29	1.5	−0.87 ± 0.22
Pristine_112.5667+45.9455	07:30:16.02	+45:56:44	13.20	−67.3	6400	3.85	1.5	−0.76 ± 0.15
Pristine_112.6119+45.7784	07:30:26.88	+45:46:42	12.24	+22.1	6266	4.13	1.5	−0.77 ± 0.16
Pristine_113.0244+45.6965	07:32:05.86	+45:41:47	14.49	−19.4	6165	4.00	1.5	−0.13 ± 0.26
Pristine_113.4132+41.9324	07:33:39.19	+41:55:57	14.08	+1.0	6183	4.00	1.5	−1.02 ± 0.24
Pristine_113.4275+45.6423	07:33:42.62	+45:38:32	14.35	−13.9	6410	4.00	1.5	−0.49 ± 0.31
Pristine_113.6421+45.4681	07:34:34.12	+45:28:06	14.11	+8.6	6043	3.90	1.3	−0.58 ± 0.18
Pristine_180.8898+15.6500	12:03:33.55	+15:39:00	12.97	+15.7	6500	4.10	1.5	−1.71 ± 0.17
Pristine_180.8994+16.3260	12:03:35.88	+16:19:34	11.77	−17.8	4970	2.36	2.0	−1.04 ± 0.13
Pristine_181.4437+13.4888	12:05:46.50	+13:29:20	13.15	−45.7	6097	4.43	1.3	−0.88 ± 0.15
Pristine_182.2972+13.1228	12:09:11.35	+13:07:22	12.69	+92.0	6521	4.39	1.5	−1.46 ± 0.17
Pristine_183.1390+16.1839	12:12:33.34	+16:11:02	13.26	−13.0	5130	3.54	1.0	−0.51 ± 0.15
Pristine_183.4550+17.0927	12:13:49.22	+17:05:34	13.38	+40.8	6725	3.83	1.5	−0.82 ± 0.12
Pristine_185.5596+15.5893	12:22:14.32	+15:35:21	13.85	+36.6	6463	4.28	1.5	−1.22 ± 0.15
Pristine_188.4543+15.1750	12:33:49.02	+15:10:30	12.60	+10.9	6072	4.10	1.3	−0.46 ± 0.15
Pristine_191.9208+16.0031	12:47:40.99	+16:00:11	12.79	+11.8	5433	2.35	1.5	−1.23 ± 0.14
Pristine_192.4508+12.7922	12:49:48.20	+12:47:54	13.44	−8.3	6262	4.12	1.5	−1.38 ± 0.14
Pristine_193.5777+10.3945	12:54:18.66	+10:23:41	14.10	−68.9	6300	4.55	1.5	−1.74 ± 0.21
Pristine_195.1494+06.5655	13:00:35.82	+06:33:56	12.37	+352.7	5370	2.80	1.5	−2.35 ± 0.24
Pristine_198.3167+14.9688	13:13:16.02	+14:58:08	13.12	10.8	6410	4.36	1.5	−0.59 ± 0.13
Pristine_206.8050+00.7423	13:47:13.20	+00:44:32	12.89	+59.4	5482	3.10	1.5	−1.92 ± 0.23
Pristine_206.9304+11.8894	13:47:43.29	+11:53:22	13.69	+72.5	6409	4.48	1.5	−1.18 ± 0.32
Pristine_212.2541+11.4580	14:09:00.98	+11:27:29	12.80	−146.0	4514	1.05	2.0	−1.67 ± 0.35
Pristine_213.1910+14.7927	14:12:45.85	+14:47:34	13.94	−61.2	5100	1.90	2.0	−2.81 ± 0.17
Pristine_216.1506+14.1298	14:24:36.14	+14:07:47	14.56	−52.6	5754	2.50	1.5	−1.32 ± 0.33
Pristine_234.0338+12.6370	15:36:08.10	+12:38:13	13.01	−170.8	6603	4.20	1.5	−2.49 ± 0.08
Pristine_235.0278+07.5059	15:40:06.65	+07:30:21	13.79	+65.7	6442	3.13	1.5	−1.12 ± 0.34
Pristine_235.0537+07.5988	15:40:12.89	+07:35:56	13.73	−126.7	6680	4.32	1.5	−2.19 ± 0.13
Pristine_236.4719+15.3328	15:45:53.24	+15:19:58	14.25	−142.5	6444	4.35	1.5	−1.75 ± 0.21
Pristine_236.7635+05.4474	15:47:03.25	+05:26:51	13.19	−213.2	5370	2.94	1.5	−2.03 ± 0.17
Pristine_238.2716+07.5917	15:53:05.17	+07:35:30	14.42	−86.1	5202	2.48	1.8	−2.32 ± 0.22
Pristine_240.2908+07.9401	16:01:09.79	+07:56:24	13.87	−0.5	5023	1.78	2.0	−2.16 ± 0.24
Pristine_241.1299+06.3632	16:04:31.16	+06:21:48	14.12	−159.9	6269	4.00	1.5	−1.57 ± 0.20
Pristine_246.4406+15.0900	16:25:45.74	+15:05:24	13.75	+107.5	6081	2.63	1.5	−1.59 ± 0.17
Multiple systems								
Pristine_111.9501+44.1449	07:27:48.06	+44:08:42	13.49					
Pristine_113.6058+45.8841	07:34:25.39	+45:53:03	12.52					
Pristine_230.2650+00.9137	15:21:03.59	+00:54:49	12.19					
F stars and stars with low S/N spectra								
Pristine_113.6744+45.8738	07:34:41.87	+45:52:26	14.29	+92.5				
Pristine_219.0145+11.6057	14:36:03.46	+11:36:20	14.02	−4.0				
Pristine_232.8856+07.8678	15:31:32.54	+07:52:04	12.91	−82.4				
Pristine_237.8581+07.1456	15:51:25.96	+07:08:44	13.73	−50.0				

[a] J2000, from Gaia DR2
The number after the ± next to [Fe/H] is the line-to-line scatter.

Table 3. Chemical abundances of iron, sodium, magnesium, aluminium, silicon and sulphur.

Star	A(Fe I)	A(Fe II)	A(Na)	A(Mg)	A(Al)	A(Si I)	A(Si II)	A(S)
Pristine_110.0459+43.0522	5.10 ± 0.28	4.69 ± 0.08		5.36 ± 0.23				
Pristine_110.4208+40.8947	5.95 ± 0.40	5.54	4.54	6.43 ± 0.71				
Pristine_111.5919+44.0179	6.82 ± 0.20	6.79 ± 0.25	5.79	7.05 ± 0.05				
Pristine_112.0456+43.9914	6.99 ± 0.24	7.14 ± 0.42		7.15 ± 0.20				
Pristine_112.3237+44.2279	6.65 ± 0.15	6.59 ± 0.17	5.42	6.97 ± 0.16		6.96	7.05	
Pristine_112.5667+45.9455	6.76 ± 0.22	6.77 ± 0.12	5.88 ± 0.22	6.99 ± 0.13			7.21	
Pristine_112.6119+45.7784	6.75 ± 0.16	6.74 ± 0.18		7.11 ± 0.15		7.12		
Pristine_113.0244+45.6965	7.39 ± 0.26	7.43 ± 0.30		7.57 ± 0.05				
Pristine_113.4132+41.9324	6.50 ± 0.24	6.25 ± 0.26		6.91 ± 0.12				
Pristine_113.4275+45.6423	7.03 ± 0.31	7.10 ± 0.51	6.14	7.26 ± 0.20				
Pristine_113.6421+45.4681	6.94 ± 0.18	6.88 ± 0.16	5.57	7.05 ± 0.16				
Pristine_113.7050+45.5860	6.95 ± 0.25	6.92 ± 0.30		6.98 ± 0.15				
Pristine_180.0750+16.3239	7.48 ± 0.16	7.48 ± 0.16	6.60 ± 0.18	7.45 ± 0.15	6.81	7.68 ± 0.14	7.82 ± 0.01	7.70
Pristine_180.8898+15.6500	5.81 ± 0.17	5.61 ± 0.14		6.16 ± 0.13		6.98		
Pristine_180.8994+16.3260	6.48 ± 0.13	6.37 ± 0.18		6.91 ± 0.18				
Pristine_181.4437+13.4888	6.64 ± 0.15	6.44 ± 0.12	5.63 ± 0.15	7.12 ± 0.11		6.85 ± 0.01		
Pristine_182.2972+13.1228	6.06 ± 0.17	5.84 ± 0.15		6.40 ± 0.15				
Pristine_183.1390+16.1839	7.01 ± 0.15	6.66 ± 0.25	5.99 ± 0.09	7.33 ± 0.26		7.24 ± 0.15		
Pristine_183.4550+17.0927	6.70 ± 0.12	6.77 ± 0.10	5.73	7.21 ± 0.10		7.00	7.03	
Pristine_185.5596+15.5893	6.30 ± 0.15	6.07 ± 0.10		6.83 ± 0.20				
Pristine_188.4543+15.1750	7.09 ± 0.15	7.06 ± 0.21	5.95 ± 0.11	7.36 ± 0.25		7.23 ± 0.14	7.51	
Pristine_191.9208+16.0031	6.29 ± 0.14	6.17 ± 0.13	5.02	6.79 ± 0.13		6.57		
Pristine_192.4508+12.7922	6.14 ± 0.14	6.02 ± 0.13		6.67 ± 0.19				
Pristine_193.5777+10.3945	5.78 ± 0.21	5.52 ± 0.09	4.52	6.26 ± 0.28				
Pristine_195.1494+06.5655	5.17 ± 0.24	5.04 ± 0.14	3.77	5.60 ± 0.14		7.04		
Pristine_198.3167+14.9688	6.93 ± 0.13	6.81 ± 0.15	5.84 ± 0.06	7.20 ± 0.21			6.99	
Pristine_206.8050+00.7423	5.60 ± 0.23	5.74 ± 0.65		6.03 ± 0.21				
Pristine_206.9304+11.8894	6.34 ± 0.32	6.30		6.58 ± 0.08				
Pristine_212.2541+11.4580	5.85 ± 0.35	5.80 ± 0.49		6.83 ± 0.39				
Pristine_213.1910+14.7927	4.71 ± 0.17	5.00		5.03 ± 0.39				
Pristine_216.1506+14.1298	6.20 ± 0.33	6.09 ± 0.08		6.41 ± 0.35				
Pristine_234.0338+12.6370	5.03 ± 0.08	4.80 ± 0.13		5.45 ± 0.12				
Pristine_235.0278+07.5059	6.40 ± 0.34	6.59 ± 0.11		7.01 ± 0.32				
Pristine_235.0537+07.5988	5.33 ± 0.13	5.12 ± 0.04		5.74 ± 0.06				
Pristine_236.4719+15.3328	5.77 ± 0.21	5.60 ± 0.23	4.92	6.07 ± 0.11				
Pristine_236.7635+05.4474	5.49 ± 0.17	5.34 ± 0.25		5.98 ± 0.10				
Pristine_238.2716+07.5917	5.20 ± 0.22	4.93 ± 0.29	3.87	5.47 ± 0.24				
Pristine_240.2908+07.9401	5.36 ± 0.24	5.26 ± 0.34		5.95 ± 0.35				
Pristine_241.1299+06.3632	5.95 ± 0.20	5.91 ± 0.18		6.38 ± 0.12				
Pristine_246.4406+15.0900	5.93 ± 0.17	6.10 ± 0.31						

The number after the ± next to an abundance is the line-to-line scatter,
if there is none the abundance has been derived from a single line.

3.3 Pristine_230.2650+00.9137

This system was observed only on April 16^{th} 2018, barycentric julian date 2458224.5458990 and its cross correlation function shows two clear peaks at –110.4 km s^{-1} and –68.4 km s^{-1}. The Gaia DR2 reports a radial velocity for this star of –85.1 km s^{-1} with an error of 5.9 km s^{-1} for an epoch of 2015.5 and with only five radial velocity measurements. This radial velocity is compatible, within errors, with the center of mass velocity of the system derived from our measurements of -89.4 km s^{-1}. It should be noted that for a star of this magnitude (G = 12.02) the expected error on the radial velocity is less than 3 km s^{-1}(Sartoretti et al. 2018). The fact that the error is larger than this supports the notion that the stars displays radial velocity variations. At the end of the mission the accumulated data should allow to determine a spectroscopic orbit. The system has a companion at 0.″01 in the Gaia DR2 data. Star Gaia DR2 4420599693613027456 has G=20.8 and $G_{BP} - G_{RP}$=0.557, it has no parallax or proper motion measurement. The star is too faint to be responsible for the secondary line system visible in our spectrum. If it were gravitationally bound to Pristine_230.2650+00.9137 at the distance of 308 pc, as derived from the Gaia parallax, its angular separation implies a linear separation of about 3 pc. Its colour is too blue to be an M dwarf, so if it were physically bound to Pristine_230.2650+00.9137 it could only be a white dwarf to explain the difference in luminosity. With the above considerations we believe it is more likely that it is just a fortuitous alignment and Gaia DR2 4420599693613027456 and Pristine_230.2650+00.9137 are not gravitationally bound. However the Gaia end of mission data should be able to provide at least a proper motion for Gaia DR2 4420599693613027456

Table 4. Chemical abundances of calcium to manganese.

Star	A(Ca)	A(Sc)	A(Ti I)	A(Ti II)	A(V)	A(Cr I)	A(Cr II)	A(Mn)
Pristine_110.0459+43.0522	4.32			2.62 ± 0.31		2.66 ± 0.12		
Pristine_110.4208+40.8947	5.12 ± 0.49			4.64		4.38 ± 0.93		
Pristine_111.5919+44.0179	6.04 ± 0.17	2.79 ± 0.21	4.32 ± 0.12	4.73 ± 0.32		4.96 ± 0.18		4.91
Pristine_112.0456+43.9914	6.26 ± 0.30	3.16		5.09 ± 0.27		5.10 ± 0.14	5.89 ± 0.28	
Pristine_112.3237+44.2279	5.71 ± 0.16	2.44 ± 0.20	4.22 ± 0.10	4.39 ± 0.16		4.76 ± 0.11	4.97 ± 0.09	4.69 ± 0.19
Pristine_112.5667+45.9455	5.86 ± 0.16	2.73 ± 0.08	4.27 ± 0.30	4.47 ± 0.18		4.92 ± 0.10	$4.88\pm$	4.45 ± 0.02
Pristine_112.6119+45.7784	5.92 ± 0.16	2.64 ± 0.09	4.28 ± 0.21	4.51 ± 0.22		4.93 ± 0.24	4.84 ± 0.03	4.86 ± 0.07
Pristine_113.0244+45.6965	6.44 ± 0.22					4.78		
Pristine_113.4132+41.9324	5.64 ± 0.22	2.43 ± 0.06	4.41 ± 0.05	4.35 ± 0.21		4.64 ± 0.03		
Pristine_113.4275+45.6423	6.02 ± 0.31	2.82	4.62	4.90 ± 0.60		4.90 ± 0.13		
Pristine_113.6421+45.4681	6.06 ± 0.18	2.82 ± 0.20	4.62 ± 0.34	4.89 ± 0.36		5.25 ± 0.25	5.27 ± 0.01	4.98 ± 0.23
Pristine_113.7050+45.5860	6.01 ± 0.25	2.94		4.83 ± 0.14		5.06 ± 0.02		
Pristine_180.0750+16.3239	6.43 ± 0.15	3.62	5.00 ± 0.21	4.80 ± 0.14	4.10 ± 0.05	5.60 ± 0.15	5.53 ± 0.08	5.60 ± 0.15
Pristine_180.8898+15.6500	5.08 ± 0.11	1.57 ± 0.15	3.60 ± 0.22	3.67 ± 0.17		3.85 ± 0.15		
Pristine_180.8994+16.3260	5.66 ± 0.10		4.25 ± 0.10	4.10 ± 0.15				4.47
Pristine_181.4437+13.4888	5.80 ± 0.11	2.42 ± 0.29	4.41 ± 0.09	4.40 ± 0.11		4.80 ± 0.07	4.72	4.38 ± 0.11
Pristine_182.2972+13.1228	5.15 ± 0.15	1.86 ± 0.11	3.82 ± 0.11	3.83 ± 0.18		4.20 ± 0.19		
Pristine_183.1390+16.1839	6.26 ± 0.15	2.95 ± 0.16	4.87 ± 0.11	4.65 ± 0.25	3.88 ± 0.15	5.30 ± 0.13	4.95 ± 0.25	5.12 ± 0.16
Pristine_183.4550+17.0927	5.87 ± 0.12	2.76 ± 0.21	4.39 ± 0.22	4.58 ± 0.10		4.95 ± 0.21	4.82 ± 0.01	4.50
Pristine_185.5596+15.5893	5.50 ± 0.11	2.23 ± 0.11	4.07 ± 0.19	4.10 ± 0.09		4.32 ± 0.09		
Pristine_188.4543+15.1750	6.13 ± 0.12	2.84 ± 0.18	4.69 ± 0.22	4.75 ± 0.17		5.29 ± 0.09	5.24 ± 0.20	5.13 ± 0.07
Pristine_191.9208+16.0031	5.38 ± 0.15	2.08 ± 0.09	3.97 ± 0.10	4.05 ± 0.16		4.33 ± 0.12	4.20 ± 0.06	3.94 ± 0.13
Pristine_192.4508+12.7922	5.37 ± 0.16	2.03 ± 0.05	3.98 ± 0.18	4.08 ± 0.11		4.27 ± 0.17		
Pristine_193.5777+10.3945	5.02 ± 0.09	1.42		3.50 ± 0.20		3.79 ± 0.17		
Pristine_195.1494+06.5655	4.49 ± 0.24			2.90 ± 0.18		3.23 ± 0.43		
Pristine_198.3167+14.9688	5.97 ± 0.12	2.58 ± 0.13	4.53 ± 0.06	4.54 ± 0.14		5.07 ± 0.05	5.03 ± 0.08	4.96 ± 0.04
Pristine_206.8050+00.7423	4.73 ± 0.22			3.74 ± 0.19		3.48 ± 0.10		
Pristine_206.9304+11.8894	5.51							
Pristine_212.2541+11.4580	4.77 ± 0.25	1.67	3.74 ± 0.41	3.43 ± 0.41		4.29 ± 0.46		
Pristine_213.1910+14.7927	4.36							
Pristine_216.1506+14.1298	5.52 ± 0.35	2.36 ± 0.20		4.24 ± 0.38		4.15 ± 0.25		
Pristine_234.0338+12.6370	4.56	0.82		2.87 ± 0.08		3.08		
Pristine_235.0278+07.5059	5.37 ± 0.11	2.44 ± 0.46	$3.93\pm$	4.36 ± 0.35		4.93 ± 0.49	4.61	
Pristine_235.0537+07.5988	4.43 ± 0.09	1.01		3.07 ± 0.11			3.59	
Pristine_236.4719+15.3328	4.89 ± 0.22			3.72 ± 0.25		3.60 ± 0.03		
Pristine_236.7635+05.4474	4.69 ± 0.20	1.36 ± 0.19	3.20 ± 0.11	3.24 ± 0.12		3.43 ± 0.09		
Pristine_238.2716+07.5917	4.47			3.01 ± 0.09		3.39 ± 0.77		
Pristine_240.2908+07.9401	4.73 ± 0.37	1.61 ± 0.61	3.02 ± 0.20	3.10 ± 0.09		3.14 ± 0.09		
Pristine_241.1299+06.3632	5.30 ± 0.21	1.26		3.83 ± 0.18		3.77 ± 0.18		
Pristine_246.4406+15.0900	5.26 ± 0.41	1.65	3.56 ± 0.03	3.71 ± 0.17			4.28 ± 0.21	

The number after the $\pm$ next to an abundance is the line-to-line scatter, if there is none the abundance has been derived from a single line.

and that will allow to decide if the two are a common proper motion pair.

4 CHEMICAL ANALYSIS

4.1 Atmospheric parameters

To derive the stellar parameters, we used Gaia DR2. Reddennings were derived from the maps of Green et al. (2018a). By using the parallax, we derived the absolute G magnitude [2]. This latter value combined with the Gaia $(G_{BP} - G_{RP})$ colour was compared to PARSEC (Bressan et al. 2012; Marigo et al. 2017) isochrones of metallicity close to the metallicity estimate, in order to derive the effective temperature ($T_{\rm eff}$) and the surface gravity ($\log g$) of each star (see e.g. Fig. 2). This procedure can require few iterations: the metallicity of the isochrones first to compare to the star's photometry is initially taken from the photometric estimate (Starkenburg et al. 2017); with the derived $T_{\rm eff}$ and $\log g$ a new metallicity is obtained from the spectrum analysis; if this latter values is different from the initial guess, the comparison with isochrones of closer metallicities is repeated. The Gaia parallax is very good (relative error less than 10%) for 85% of our sample (40 stars). Only two stars have a relative error on the parallax larger than 30%: Pristine_213.1910+14.7927 (relative error of 35%) and Pristine_212.2541+11.4580 (relative error of 51%). Unsurprisingly these two stars are the most distant since they are giants. The red giant branches of different metallicity are very closely packed in the colour magnitude diagram, im-

[2] $G_{abs} = G + 5 + 5\log(\varpi)$

Table 5. Chemical abundances of cobalt to barium.

Star	A(Co)	A(Ni)	A(Cu)	A(Zn)	A(Sr)	A(Y)	A(Zr)	A(Ba)
Pristine_110.0459+43.0522								
Pristine_110.4208+40.8947					2.34			1.00
Pristine_111.5919+44.0179		5.51			2.87 ± 0.09			1.78 ± 0.38
Pristine_112.0456+43.9914		5.82 ± 0.21			2.84			1.89 ± 0.20
Pristine_112.3237+44.2279		5.47 ± 0.17		3.77	2.54	1.04		1.59 ± 0.10
Pristine_112.5667+45.9455		5.45 ± 0.09		4.02	2.94	1.51 ± 0.09		1.84 ± 0.40
Pristine_112.6119+45.7784		5.53 ± 0.13		3.96	2.82 ± 0.33			1.83
Pristine_113.0244+45.6965								
Pristine_113.4132+41.9324		5.21			2.29			1.44 ± 0.01
Pristine_113.4275+45.6423		5.49			2.27 ± 0.41			1.97 ± 0.26
Pristine_113.6421+45.4681		5.65 ± 0.16			3.24			1.94 ± 0.09
Pristine_113.7050+45.5860					2.60			2.18
Pristine_180.0750+16.3239	5.28	6.32 ± 0.20		4.55	2.88	1.89 ± 0.04		2.08 ± 0.14
Pristine_180.8898+15.6500		4.59			1.23			0.84 ± 0.22
Pristine_180.8994+16.3260		5.31 ± 0.02			2.34			1.15 ± 0.20
Pristine_181.4437+13.4888		5.38 ± 0.21		3.82 ± 0.04				1.48 ± 0.13
Pristine_182.2972+13.1228		4.71			1.75 ± 0.18			0.82 ± 0.20
Pristine_183.1390+16.1839	5.29	5.80 ± 0.21	4.15 ± 0.49	4.06 ± 0.41	2.63	1.49 ± 0.27	2.44	1.82 ± 0.23
Pristine_183.4550+17.0927		5.50 ± 0.11		3.93	2.65	1.20		1.57 ± 0.19
Pristine_185.5596+15.5893		5.03 ± 0.03			1.73			1.05 ± 0.14
Pristine_188.4543+15.1750		5.84 ± 0.17	3.80	4.30	2.55	1.32 ± 0.14		1.88 ± 0.11
Pristine_191.9208+16.0031		5.03 ± 0.16	2.83	3.39 ± 0.03	2.14	0.62 ± 0.01		1.21 ± 0.05
Pristine_192.4508+12.7922		4.93 ± 0.02			2.11	1.05		1.15 ± 0.03
Pristine_193.5777+10.3945								0.50
Pristine_195.1494+06.5655		3.64			1.40 ± 0.42			−0.10 ± 0.26
Pristine_198.3167+14.9688		5.64 ± 0.14		3.89 ± 0.08	2.71	1.43		1.75 ± 0.18
Pristine_206.8050+00.7423		4.15						0.39 ± 0.29
Pristine_206.9304+11.8894								1.29
Pristine_212.2541+11.4580		4.70 ± 0.42						0.54
Pristine_213.1910+14.7927								
Pristine_216.1506+14.1298					1.97			1.15 ± 0.33
Pristine_234.0338+12.6370					0.28			1.04
Pristine_235.0278+07.5059		5.16						2.21
Pristine_235.0537+07.5988					1.05			
Pristine_236.4719+15.3328								0.67 ± 0.11
Pristine_236.7635+05.4474		4.18			1.15 ± 0.08			0.33 ± 0.20
Pristine_238.2716+07.5917		4.02			0.81			0.07 ± 0.21
Pristine_240.2908+07.9401		3.87						−0.29 ± 0.10
Pristine_241.1299+06.3632		4.79			1.86			0.84 ± 0.22
Pristine_246.4406+15.0900						0.49 ± 0.22		

The number after the ± next to an abundance is the line-to-line scatter, if there is none the abundance has been derived from a single line.

plying that the surface gravity estimate obtained with our procedure is in this case robust against errors in the parallax. Changing the absolute magnitude of either star by what implied by a change of $\pm 1\sigma$ in the parallax would place the star far from any isochrone in the colour-magnitude diagram. Furthermore the metallicity is derived from the mean Fe I abundance, that is only very little affected by the adopted surface gravity. This fact also contributes to make our procedure robust against errors in the parallax.

We checked our derived $T_{\rm eff}$ against the temperatures derived using the Infrared Flux Method, as implemented by González Hernández & Bonifacio (2009), using 2MASS JHK photometry. We find the two sets of temperature are very well correlated and compatible within errors. A linear fit provides $T_{\rm eff}(adopted) = 1.0285 \times T_{\rm eff}(IRFM) - 39.8\,K$, with an r.m.s around the fit of 105 K. We take this external comparison as representative of the systematic uncertainty in our effective temperatures. The uncertainties linked to the uncertainty in the Gaia photometry are negligible with respect to this.

For the majority of the stars, the age of the isochrone matching the photometry of the stars was larger than about 7 Gyr, and it was for all but four stars, larger than 5.5 Gyr. Pristine_195.1494+06.5655 is an evolved star, with [Fe/H] = −2.35. When we compare its Gaia photometry to an isocrone of −2.0 metallicity, we find that the star fit well for an age of 2.5 Gyr (see Fig. 3), this is strange for a metal-poor star. But at this stage in evolution, a slightly smaller reddening would reconcile the star with an older isochrone, we therefore do not consider its age estimate robust. The next youngest star is Pristine_113.7050+45.5860 (Age=3.5 Gyr), with [Fe/H] = −0.57, that has an orbit consistent with the thin disc (see Sect. 5.1). Pristine_183.4550+17.0927 ([Fe/H] = −0.82) and Pristine_206.9304+11.8894 ([Fe/H] = −1.18) are consistent

Table 6. Variations in abundances, in the sense "adopted" – "new value", for star Pristine_183.4550+17.0927 as a result of a change in one of the atmospheric parameters.

Abundance	$T_{\rm eff}$ +100 K	$T_{\rm eff}$ –100 K	log g +0.3 dex	log g -0.3 dex	ξ +0.2 km s^{-1}
A(Na I)	−0.06	+0.07	−0.02	+0.04	+0.03
A(Mg I)	−0.11	+0.12	−0.09	+0.14	+0.05
A(Si I)	+0.01	−0.01	+0.06	−0.06	+0.02
A(Ca I)	−0.09	+0.10	−0.03	+0.08	+0.07
A(Sc II)	−0.02	+0.05	+0.16	−0.15	+0.10
A(Ti I)	−0.12	+0.13	−0.02	+0.02	+0.08
A(Ti II)	−0.03	+0.03	+0.09	−0.10	+0.07
A(V I)	−0.12	+0.13	+0.00	+0.00	+0.01
A(Cr I)	−0.10	+0.14	−0.01	+0.06	+0.10
A(Cr II)	+0.06	−0.05	+0.15	−0.14	+0.09
A(Mn I)	−0.02	+0.09	+0.06	+0.06	+0.15
A(Fe I	−0.09	+0.10	−0.03	+0.04	+0.09
A(Fe II)	+0.02	−0.02	+0.12	−0.16	+0.10
A(Co I)	−0.05	+0.04	+0.05	−0.07	+0.15
A(Ni I)	−0.07	+0.06	+0.02	−0.02	+0.08
A(Cu I)	−0.05	+0.11	+0.05	+0.02	+0.10
A(Zn I)	−0.01	+0.02	+0.08	−0.08	+0.07
A(Sr II)	−0.02	+0.02	+0.10	−0.12	+0.03
A(Y II)	+0.00	+0.00	+0.18	−0.18	+0.15
A(Zr II)	−0.01	+0.06	+0.15	−0.17	+0.05
A(Ba II)	−0.04	+0.04	+0.10	−0.10	+0.19

with an age of 4 Gyr. They both seem too young to be this metal-poor (see Fig. 3). In fact the Milky Way essentially shut down its vigourous star formation 9 Gyr ago, to start again forming stars at a lower rate at the time of the formation of the thin disc (Haywood et al. 2016), thus the young age of these stars suggests that they belong to the thin disc, while their kinematics and metallicity is consistent with the thick disc (see Sect. 5.1 They could be blue stragglers, like HR 3220 (Fuhrmann & Bernkopf 1999), but we note that stars that are young, metal-poor and α enhanced have also been pointed out by Haywood et al. (2013, see their figure 17), Martig et al. (2015) and Chiappini et al. (2015). A young age and low metallicity may also be the sign of stars that have been formed in satellite galaxies or clusters and then accreted by the Milky Way. Among the ultra faint galaxies/clusters that orbit the Milky Way there are some that are metal-poor, yet considerably younger than the bulk of the metal-poor stars in the Milky Way. One good example is Crater (Belokurov et al. 2014; Bonifacio et al. 2015; Kirby et al. 2015; Voggel et al. 2016) with a metallicity of –1.7 and an age of only 7 Gyr. Presently the existence of a galaxy/cluster, not yet detected or disrupted, with metallicity –1.0 and an age of 4 Gyr cannot be excluded.

4.2 Chemical abundancesi from atomic lines

The chemical composition of the stars was derived by using the pipeline MyGIsFOS (Sbordone et al. 2014). MyGIsFOS can be used also to derive the stellar parameters through ionisation equilibrium (to derive log g), and excitation equilibrium (for $T_{\rm eff}$), and can derive also the micro-turbulence from Fe I lines of different strength. With the quality of this sample of spectra, and also thanks to the availability of Gaia

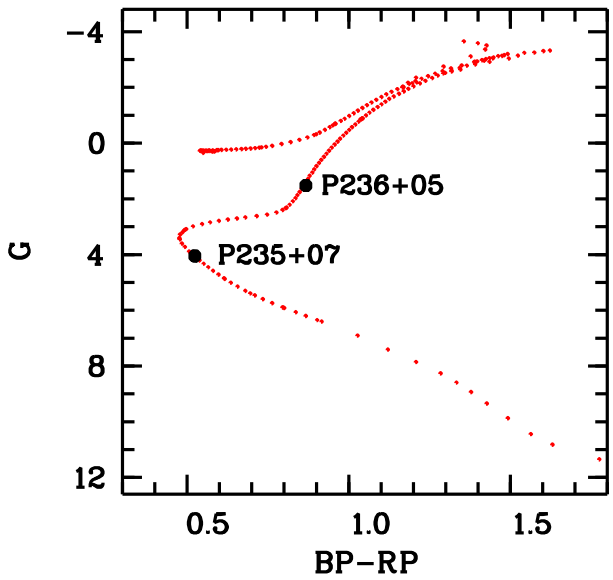

Figure 2. The comparison of the Gaia photometry to Parsec isochrones of [M/H]= −2 and an age of 9 Gyr for two metal-poor stars of the sample (Pristine_235.0537+07.5988 and Pristine_236.7635+05.4474).

DR2, we prefered to use MyGIsFOS just to derive the chemical abundances. For the micro-turbulence, due to the general low signal-to-noise ratio, no weak line could be detected, so we fixed this value in the analysis, looking at stars with similar parameters (see e.g. Cayrel et al. 2004; Bonifacio et al. 2007). For stars with $T_{\rm eff} < 5000$ K or log g < 2.0 we assumed $\xi = 2.0$ kms. For stars with 5000 K$\leq T_{\rm eff}$we adopted $\xi = 1.5$ km s^{-1}. There are five exceptions to these criteria. For Pristine_246.4406+15.0900, that is an HB star, we assumed $\xi = 1.5$. For Pristine_238.2716+07.5917, that is a warm giant, we adopted $\xi = 1.8$ km s^{-1}, rather than 1.5 km s^{-1} because this provided a better balance of FeI and FeII. For the three high metallicity F-dwarfs Pristine_113.6421+45.4681, Pristine_180.0750+16.3239 and Pristine_188.4543+15.1750, with 6000 K $\leq T_{\rm eff} \leq$6100 K we adopted $\xi = 1.3$ km s^{-1}, intermediate between that of the Sun and Procyon (Steffen et al. 2013). In Table 2 we present the coordinates for all the data sample. Stellar parameters, including [Fe/H] are provided only for the stars for which we could perform a chemical analysis. In Tables 3,4 and 5 we provide all the abundance measurements. For each element we provide the line-to-line scatter, that can be used as an error estimate. In cases for which the line-to-line scatter is less than 0.1 dex, the error is dominated by the errors due to the uncertainties in the atmospheric parameters. When only one line is measured for a given element there is no value provided. In these cases, an estimate of the statistical error could be derived from S/N in the spectrum, however one may also assume that also in these cases the error is dominated by the error on atmospheric parameters. To help estimating such errors we provide in Table 6 the variation in abundances for star Pristine_183.1390+16.1839 for changes of $\pm$100 K in $T_{\rm eff}$, $\pm$0.3 dex in log g and +0.2 km s^{-1} for ξ. In Fig. 4 the spectra, in the wavelength range of the Mg I b triplet, of the nine most metal-poor stars in the sample is shown. The quality of the spectra can be appreciated as well as the fact that even

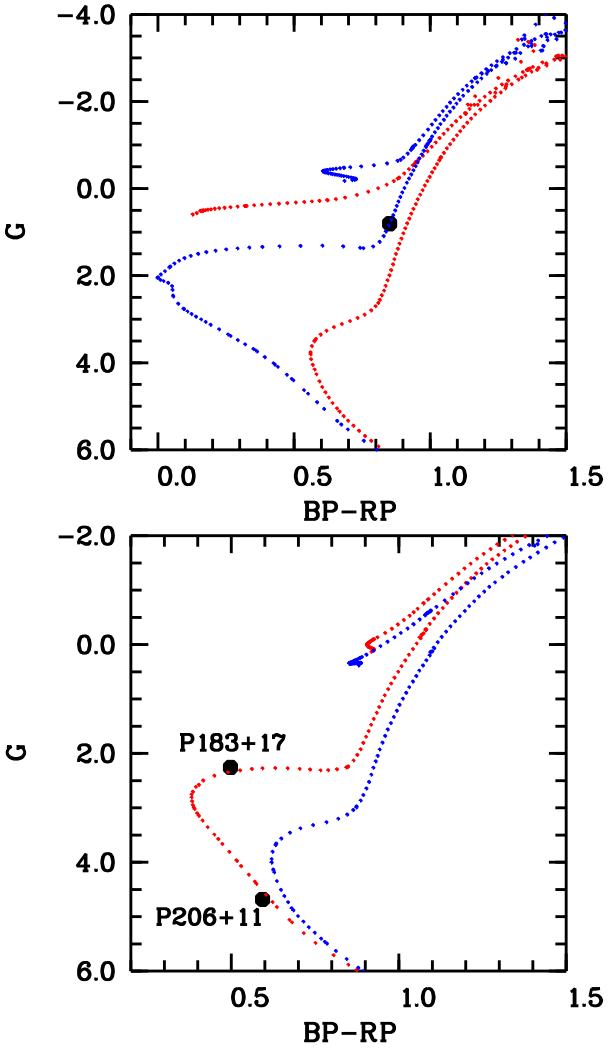

Figure 3. Upper panel: the comparison of Gaia photometry of Pristine_195.1494+06.5655 to Parsec isochrones of metallicity [M/H]= −2 for ages of 12.6 Gyr (red dots) and 2.5 Gyr (blue dots). Lower panel: the comparison of the Gaia photometry of Pristine_183.4550+17.0927 and Pristine_206.9304+11.8894 to Parsec isochrones at [M/H]= −1 for ages of 4 and 11 Gyr (red and blue, respectively).

at very low signal-to-noise ratios the Mg I b triplet lines can be measured.

The agreement between the Fe abundances derived from Fe I and Fe II lines is generally good, the mean difference A(Fe I) – A(Fe II) is 0.09 dex with a standard deviation of 0.15 dex. We note however that there is a tendency, especially at low metallicity for [Fe I/H] to be larger than [Fe II/H], this cannot be ascribed to NLTE or NLTE-3D effects, neglect of which, produces the opposite effect (Amarsi et al. 2016). This is an example that shows how a non-spectroscopic gravity does not, in general, satisfy spectroscopic diagnostic criteria. This is likely due to inadequacies in our modelling.

In Fig. 5-7 the [X/Fe] vs. [Fe/H] are shown. The solar abundances are from Lodders et al. (2009), except for S and Fe, whose solar values are from Caffau et al. (2011). The α-elements, as expected, are enhanced with respect to Fe in the metal-poor stars. The large scatter in Fig. 5 is due to the low S/N in the observed spectra. One star, Pristine_212.2541+11.8045, shows a quite large enhancement in Mg, [Mg/Fe] ~ 1. The Mg abundance is derived from three Mg I lines (470,517, and 552 nm) with a large line-to-line scatter of 0.39 dex in wavelength ranges where the S/N ratio is from 4 to 9. We think the star is in fact Mg rich, but probably less than 1 dex. The iron-peak elements, shown in Fig. 6 are, within the uncertainties, compatible with Fe.

Sr and Ba (Fig. 7) show a large scatter. According to Korotin et al. (2015), for our sample of stars the NLTE corrections for Ba are generally not large, within −0.1 dex for the unevolved stars, only for few giants the correction can be up to −0.2 or −0.3 dex. These corrections do not change the general picture of the behaviour of the Ba abundance. Two stars (Pristine_234.0338+12.6370 and Pristine_235.0278+07.5059) show a large [Ba/Fe]> 0.6. For the latter star the Ba abundance is based on one single line, the Ba II line at 649 nm with S/N=24. The Ba abundance for Pristine_235.0278+07.5059 is derived from the Ba II line at 693 nm where S/N=12.

Seven stars (Pristine_112.3237+44.2279, Pristine_180.0750+16.3239, Pristine_180.8898+15.6500, Pristine_188.4543+15.1750, Pristine_192.4508+12.7922, Pristine_234.0338+12.6370, Pristine_236.4719+15.3328), all dwarfs, show the Li doublet at 670.7 nm. The abundance we derive is uncertain due to the low S/N ratio, but, for the metal-poor stars, it is compatible with the Spite plateau (Spite & Spite 1982). Star Pristine_180.0750+16.3239 is at solar metallicity and its spectrum shows a strong Li feature. This is not uncommon for metal-rich stars to have a high Li abundace (see e.g. Mott et al. 2017). Its A(Li)-LTE abundance is of 2.80 ± 0.10; the 3D-NLTE corretion of 0.05 (Harutyunyan et al. 2018) is small when compared to the uncertainty related to the quality of this spectrum.

Table 7. Carbon abundances for the cool stars.

Star	A(C)
Pristine_110.0459+43.0522	6.26
Pristine_110.4208+40.8947	7.09
Pristine_180.8994+16.3260	7.57
Pristine_183.1390+16.1839	8.02
Pristine_191.9208+16.0031	7.42
Pristine_195.1494+06.5655	6.36
Pristine_206.8050+00.7423	6.85
Pristine_212.2541+11.4580	7.04
Pristine_213.1910+14.7927	6.41
Pristine_216.1506+14.1298	6.93
Pristine_236.7635+05.4474	6.74
Pristine_238.2716+07.5917	6.24
Pristine_240.2908+07.9401	6.63

4.3 Carbon abundances from the G-band

For all the stars with $T_{\rm eff} > 5800$ K the G-band is too weak to be measurable on our spectra. For the 13 cooler stars we managed to derive the C abundance by applying an additional smoothing with a Gaussian of 10 km s^{-1} FWHM and fitting the band with synthetic spectra computed in 1D LTE. The line list adopted for the CH lines is that of

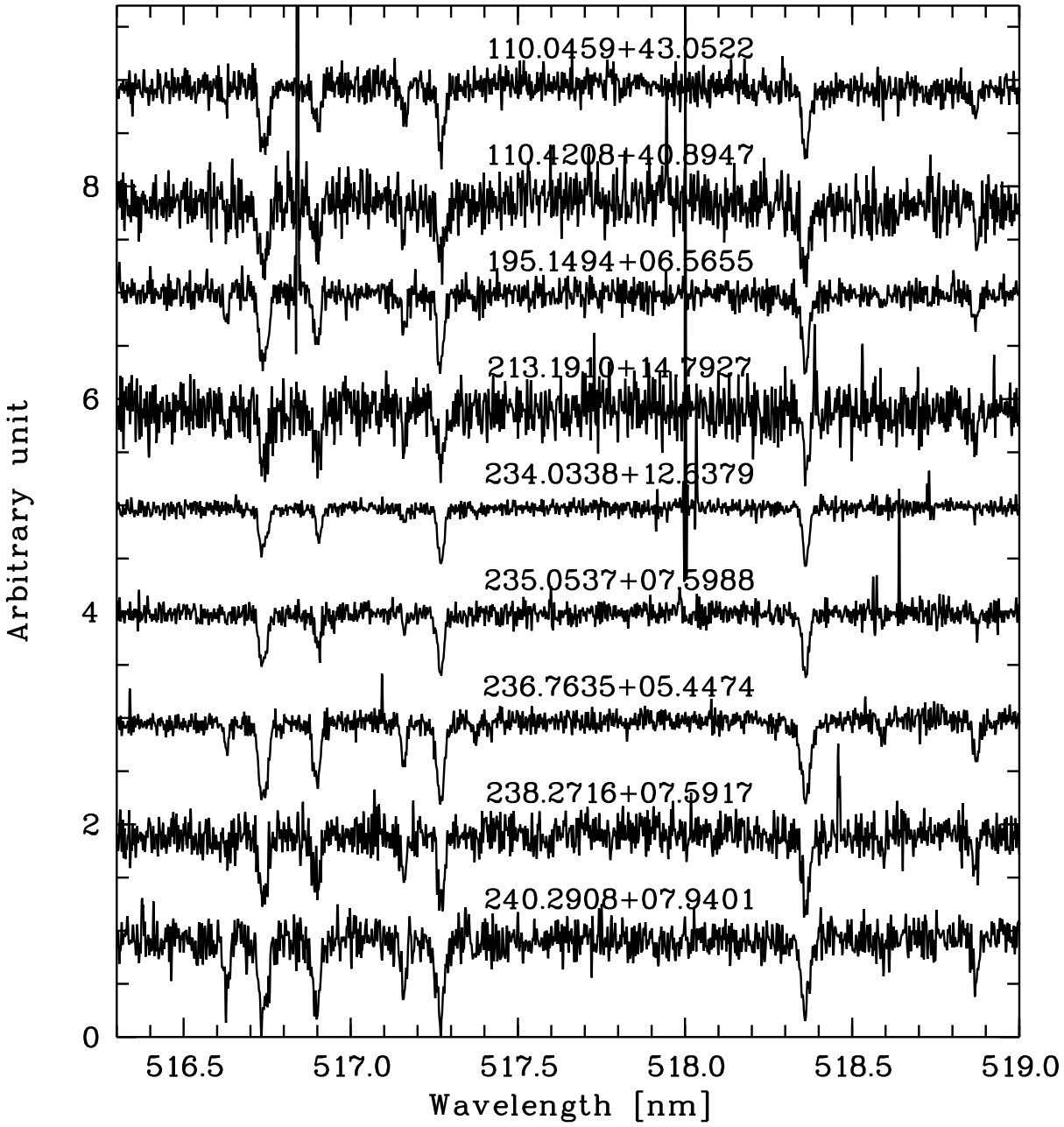

Figure 4. The Mg I b region of the observed spectra for the most metal-poor stars in the sample.

Masseron et al. (2014). The derived C abundances are provided in Table 7. The uncertainty is dominated by the continuum placement and we estimated it to be 0.3 dex for all stars. All of the stars qualify as carbon normal, according to the scheme proposed by (Bonifacio et al. 2018b).

4.4 F stars and low S/N stars

We could not derive [Fe/H] for four stars. Pristine_219.0145+11.6057 and Pristine_232.8856+07.8678 are F stars, with a sizeable $v \sin i$ in the range 15 to 30 km s^{-1}, of metallicity close to solar. Such stars are not adapted to the methods of analysis we use in this work, therefore we only provide radial velocities. Pristine_219.0145+11.6057 shows the core of Hα in emission. For Pristine_113.6744+45.8738 and Pristine_237.8581+07.14566, we have a spectrum with very poor signal-to-noise ratio and only the radial velocity is provided.

5 GALACTIC ORBITS

It is useful to use the astrometric solution from Gaia DR2 to derive distances and orbital parameters for our sample of stars. From the parallax, we first calculate the distance probability distribution function multiplying the parallax likelihood as introduced by Bailer-Jones (2015) by a proper Milky Way density profile prior that takes into account the disc and the halo component of the Galaxy as described in

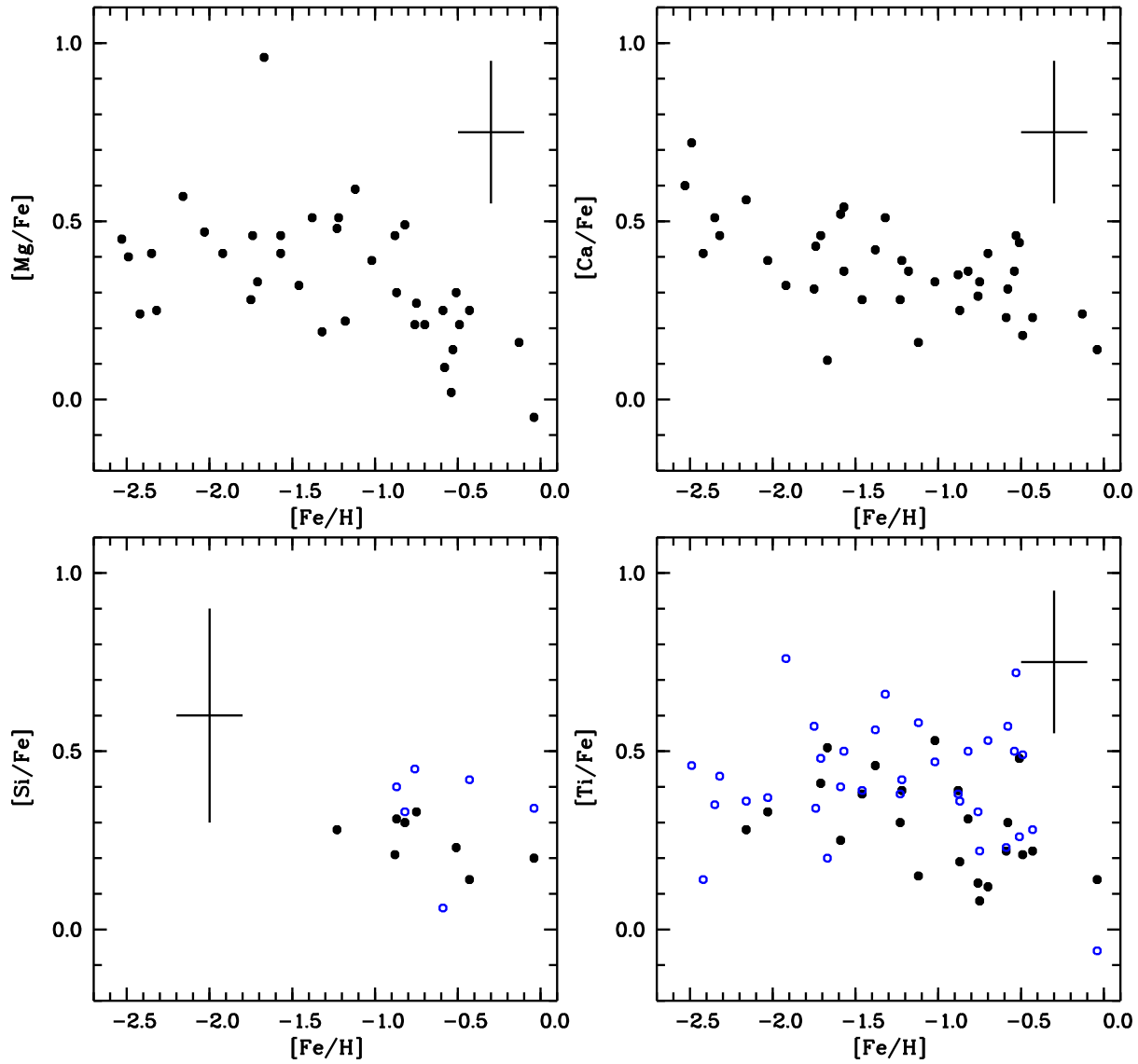

Figure 5. The α-elements: solid black are the neutral species, open blue the ionised ones.

Sestito et al. (2019). We assume as a zero offset for the parallax the value $\varpi_0 = -0.065$ mas, this is an average of the offsets found by Arenou et al. (2018b) from comparison to external catalogues of open clusters. We underline that the final classification of the orbits would have been the same even if we had not applied this offset. With the inferred distances, the radial velocities measured from high-resolution spectroscopy and the exquisite proper motion from Gaia DR2, we computed the orbital parameters using `galpy`[3] package (Bovy 2015). We use their *MWPotential14*, which is a Milky Way gravitational potential composed of a power-law, exponentially cut-off bulge, a Miyamoto Nagai Potential disc, and a Navarro et al. (1997) dark matter halo, but using a more massive halo with a mass of $1.2 \times 10^{12} M_\odot$ compatible with the value from Bland-Hawthorn & Gerhard (2016) (vs. $0.8 \times 10^{12} M_\odot$ for the halo used in *MWPotential14*). We assume that the distance between the Sun and the Galactic centre is 8.0 kpc, that the Local Standard of Rest circular velocity is $V_c = 239\,\mathrm{km\,s^{-1}}$, and that the peculiar motion of the Sun is ($U_0 = -11.10$ $\mathrm{km\,s^{-1}}$, $V_0 + V_c = 251.24\mathrm{km\,s^{-1}}$, $W_0 = 7.25\mathrm{km\,s^{-1}}$) as described in Schönrich et al. (2010, note that we changed the sign of U_0 since in our adopted system U is positive towards the Galactic anticentre).

As a check of the robustness of our derived orbits, we computed Galactic orbits also using `GravPot16` (Fernández-Trincado 2019), that assumes a semi-steady gravitational potential based on the Besançon model [4] and assuming no offset in the parallaxes. The classification of the orbits we arrive at is the same for most stars, the only noticeable exception is Pristine_216.1506+14.1298 that in this case has an unbound orbit. Even with this potential, however, making the parallax larger by 1σ turns the orbit in bound although still with a very large apocentirc distance. The space velocities and some of the quantities defining the

[3] http://github.com/jobovy/galpy

[4] https://fernandez-trincado.github.io/GravPot16/index.html

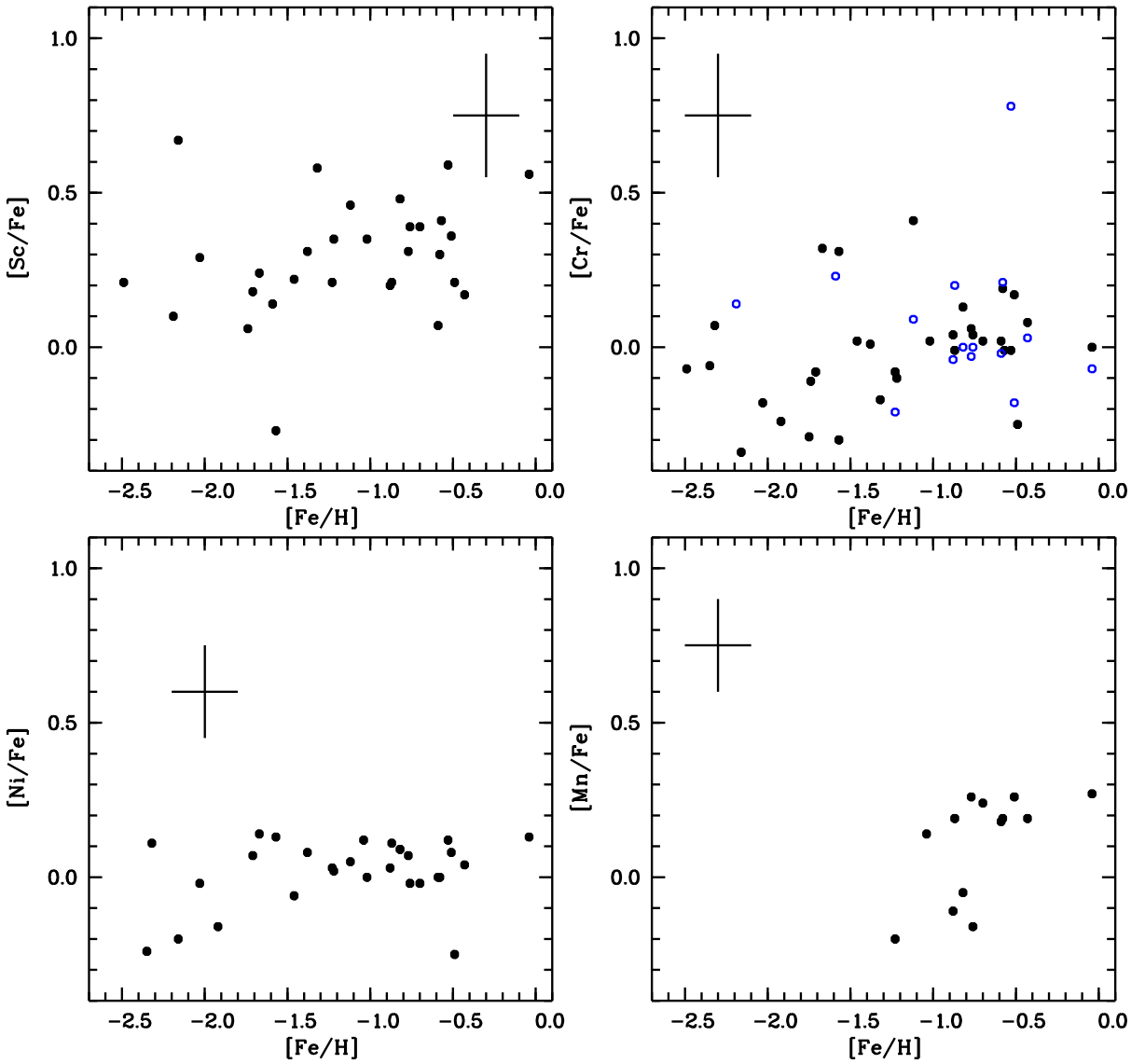

Figure 6. The elements of the Fe-peak: solid black are the neutral species, open blue the ionised ones.

Galactic orbits can be found Tables A1 and A2 in appendix A, available online.

5.1 Orbit classification

In order to investigate the relationships (if any) between chemical and kinematical properties of the stars, we decided to classify the orbits by using a minimum of assumptions on the kinematical structure of the Milky Way. We therefore decided to use as main classification parameter Z_{max}, the maximum excursion of the star from the Galactic plane and the rotational action $J_\phi/J_{\phi\odot}$, normalised to the solar value[5]. We classify as "Halo" all stars with $Z_{max} > 4$ kpc. We classify as "Thin" all stars with $Z_{max} \leq 1$ kpc and $J_\phi/J_{\phi\odot} > 0.2$. All the other stars have either 1 kpc $< Z_{max} <$ 4 or ($Z_{max} \leq 1$ kpc and $J_\phi/J_{\phi\odot} \leq 0.2$) and these we call "Thick". Note that although the names we chose are clearly suggestive of the different components of the Galaxy, our classification is purely phenomenological and based on the stellar dynamics, without any assumption as to the origin or history of any component This approach is different from what often used in the literature (see e.g. Bensby & Lind 2018), where knowledge of the kinematical parameters of each population is assumed and a probability is derived for each star to belonging to any of the assumed populations. In our case the only assumption is the underlying Galactic potential used to compute the orbits. As discussed above the use of different plausible potentials and methods of integration leads to the same classification.

Let us now examine the chemical and kinematical properties of the different classes of stars. In Fig. 8 [α/Fe], defined as the average of [Mg/Fe] and [Ca/Fe] is shown as a function of [Fe/H] and different symbols identify the different classes of stars. It is obvious that there is a trend of de-

[5] A star with $J_\phi/J_{\phi\odot} = 1$ rotates like the Sun around, the Galactic center, a low value indicates a slow rotation, a negative value a retrograde rotation

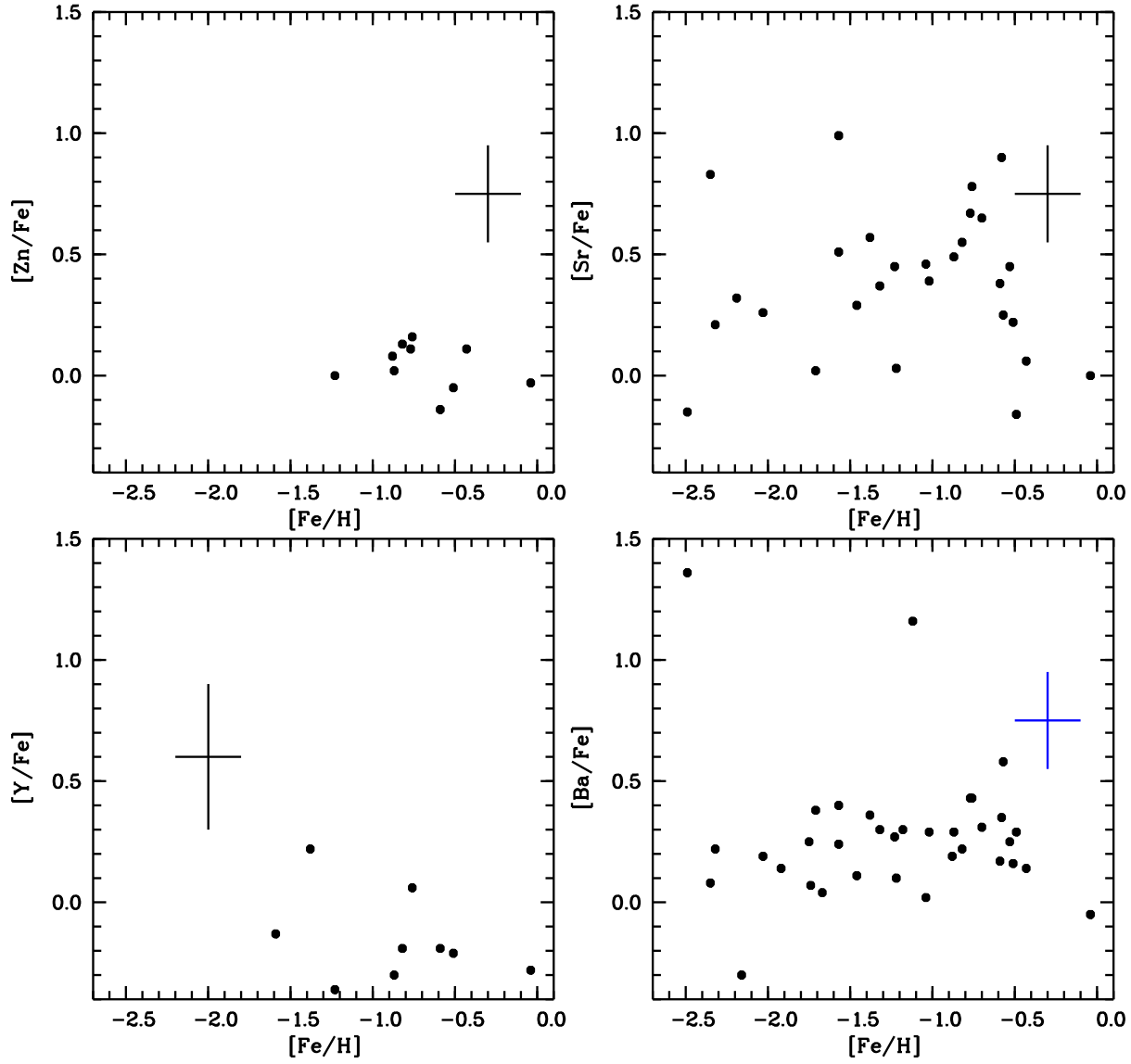

Figure 7. The heavy elements.

creasing [α/Fe] with increasing [Fe/H] both for the "Thin" stars and for the "Halo" stars. The visual perception is confirmed by the non-parametric Kendall's τ test that provides a probability of correlation of 99.87% for the "Thin" sample and 98.77% for the "Halo" sample. On the other hand the "Thick" sample shows no hint of correlation and displays a constant [α/Fe]=0.39 with a dispersion of 0.07 dex, that is far smaller than the errors on the single data points. If we ignore the presence of a trend with [Fe/H] for the "Halo" sample, we find a mean [α/Fe]=0.47 with a small dispersion of 0.08, again, much smaller than the errors on the single measurements. Considering these dispersion we cannot make a strong claim the [α/Fe] is different in the two samples, yet there is an indication. If we couple this indication with the presence of a trend with [Fe/H] for the "Halo" and none for the "Thick" we can conclude that the two samples show a different behaviour of [α/Fe]. Another feature that stands out in Fig. 8 is that the "Thin" sample extends to much lower metallicities than what are normally associated to the Thin disc and the most metal-poor stars display an α enhancement similar to that of the "Thick" sample. This, perhaps, should not come as a surprise since we know of extremely metal-poor stars such as 2MASS J1808-5104 with [Fe/H]=−3.84 (Spite et al. 2019) that is on a thin disc orbit (Schlaufman et al. 2018; Sestito et al. 2019).

In Fig. 9 we show [Fe/H] (upper panel) and [α/Fe] as a function of the apocentre distance. The "Thin" sample has on average a higher metallicity than the other two samples. It has also a considerable extension in r_{apo}, reaching out to 18 kpc. The "Thick" sample, instead, has a much wider spread in metallicity, but is not as spatially extended, it reaches out to 14.3 kpc, and half of the sample has $r_{apo} <$ 10 kpc. The "Halo" sample is the most spatialy extended.

In Fig. 10, [Fe/H] (upper panel) and [α/Fe] are shown as a function of age. Our age estimates are very crude and essentially a by-product of the parameter determination procedure, yet we believe it is worth to have a look at them. The overall trend agrees with the expectations of cosmolog-

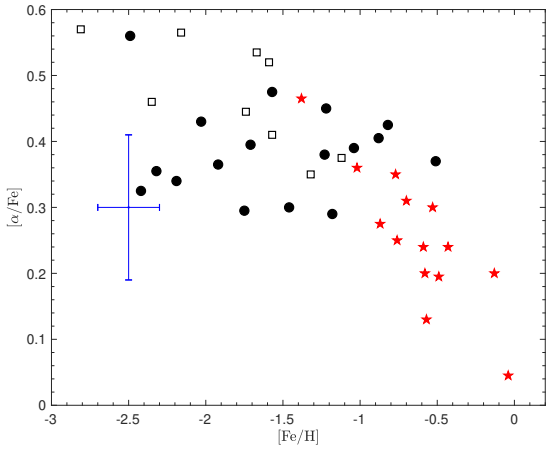

Figure 8. [α/Fe], as a function of [Fe/H]. The star symbols denote the stars classified as "Thin", the round filled symbols denote the stars classified as "Thick" and the open squares are the stars classified as "Halo".

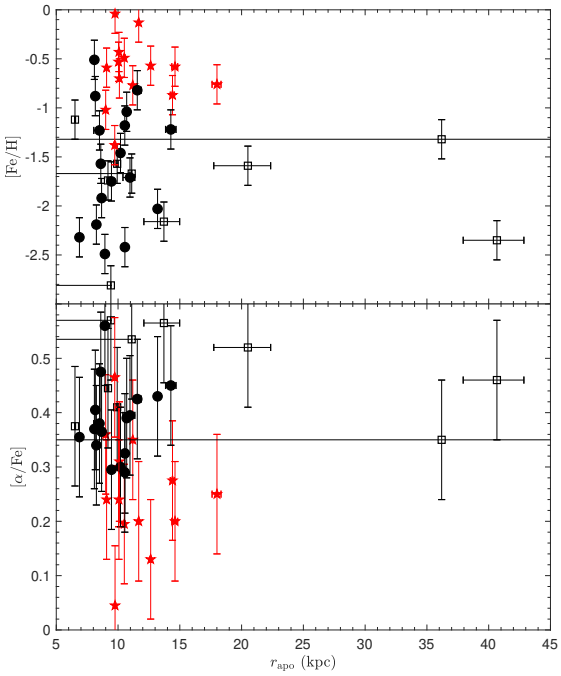

Figure 9. [Fe/H] (upper panel) and [α/Fe] (lower panel) as a function of the distance at the apogalacticon. The symbols are the same as in Fig. 8

ical chemical evolution models coupled with N-body simulation of the Milky Way formation (e.g. Salvadori et al. 2010). In the upper panel the "Thin" and "Thick" samples show a hint of an age-metallicity correlation, although, statistically, for both samples the probability of correlation is slightly less than 95% and thus should not be considered significant. What is probably more interesting is that for the "Thick" sample, at old ages there is a large dispersion in [Fe/H], which is what cosmological chemical evolution mod-

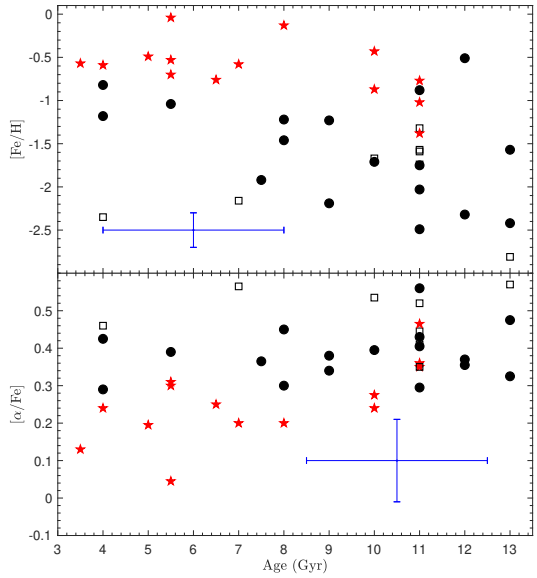

Figure 10. [Fe/H] (upper panel) and [α/Fe] (lower panel) as a function of the age. The symbols are the same as in Fig. 8

els typically predict for the early evolutionary stages (e.g. Salvadori et al. 2010) The "Halo" sample shows no hint of an age-metallicity correlation. Of the three samples only the "Thin" sample shows a clear correlation between age and [α/Fe] (99.71% probability as estimated from Kendall's τ) and, as expected, the oldest stars have the higher [α/Fe].

5.2 Shooting stars

Two of the "Halo" stars have large apocentic distances: Pristine_195.1494+06.5655 (R_{apo} = 40.7 kpc) and Pristine_216.1506+14.1298 (R_{apo} = 36.2 kpc). It is clear that with such large distances the influence of the nearby satellites of the Milky Way should be taken into account and that the stars may be in fact unbound to the Galaxy. For Pristine_216.1506+14.1298 the integration with the shallower potential used by the Besançon model and the use of the parallax at face value, without applying any offset, leads to an unbound orbit. From the chemical point of view neither of these two stars seems different from the other "Halo" stars. For Pristine_195.1494+06.5655, we already noted its possibly young age (4 Gyr), which could be easily understood if the star was formed recently in a satellite galaxy and then stripped and is currently just traversing the Milky Way (or has been accreted, if the orbit is, indeed bound).

5.3 Non-rotating old thin disc stars

Among our "Thick" sample of stars there are three that have orbits that stay very close to the Galactic disc and could therefore be considered thin disc stars. Pristine_206.9304+11.8894 (Z_{max} = 1.0 kpc), Pristine_235.0537+07.5988 (Z_{max} = 0.5 kpc) and Pristine_236.4719+15.3328 (Z_{max} = 1.0 kpc). In spite of this all three stars have very elliptical orbits and low rotational velocities. Furthermore they are all

metal-poor. Our condition on the rotational velocities places these stars in the "Thick" sample and not in the "Thin" sample. Pristine_235.0537+07.5988 and Pristine_236.4719+15.3328 are also old, while, as discussed before, Pristine_206.9304+11.8894 has an age estimate of 4 Gyr.

6 OUR NEW METHOD: COMBINING PRISTINE PHOTOMETRY WITH GAIA

The Gaia DR2 contains parallaxes (Luri et al. 2018), colours (Evans et al. 2018) and radial velocities (Sartoretti et al. 2018). The Pristine $CaHK$ magnitudes are a very powerful addition to the Gaia G, G_{BP} and G_{RP} photometry, giving extra leverage on the star's metallicity. We computed synthetic Gaia photometry, as described in Bonifacio et al. (2018a), from the Castelli & Kurucz (2003, 2004) updated grid of ATLAS 9 fluxes[6]. There are only two differences with respect to the colours provided in Bonifacio et al. (2018a): we adopted the Gaia DR2 bandpasses (Evans et al. 2018) and for the flux of Vega we used, like done for the calibration of the Gaia photometry (Evans et al. 2018), the ATLAS 9 theoretical flux of Vega of Kurucz (1993). As was explained in Starkenburg et al. (2017), the $CaHK$ magnitudes have been calibrated as AB magnitudes. In order to combine them with the Gaia magnitudes we need to transform them to Vega magnitudes. To do so we used the spectra of 582 spectrophotometric standard stars of the SDSS (York et al. 2000) that are in the Pristine footprint. We used the response function of the Ca H&K filter to compute the $CaHK$ magnitude for each of the stars, with the same zero points adopted for the synthetic photometry, and compared these magnitudes to the observed $CaHK$ magnitudes. There was no trend with colour or magnitude so the two magnitudes differ only by an offset: $CaHK_{Vega} = CaHK_{AB} + 0.18$, the error on the mean of this offset is 0.006 mag. In the following when we refer to $CaHK$ we mean on the Vegamag system.

In a way similar to what we do when combining the $CaHK$ photometry with the gri bands (Starkenburg et al. 2017; Youakim et al. 2017), we define a colour $(G - CaHK) - (G_{BP} - G_{RP})$. We decided to use this definition, rather than its inverse $(CaHK - G) - (G_{BP} - G_{RP})$ because for $T_{\rm eff}$= 6000 K the former combination spans about 5 magnitudes changing the metallicity from -4.0 to $+0.5$, but only 3 magnitudes in the latter case. The stretch in colour is illustrated in Fig. 11 where we show the synthetic colour-colour diagram, for surface gravity $\log g$= 0.5. The useful range of this colour-colour combination is for 4000 K $\leq T_{\rm eff} \leq$ 7000 K, at cooler and hotter temperatures the lines of constant metallicity cross. In this temperature range, for a given gravity, the position of the star in this diagram provides unambiguously its effective temperature and metallicity. Of course all the observed colours need to be corrected for the reddening, to do so we used the maps of Green et al. (2018b) and the Gaia parallaxes to estimate the distances. The iterative procedure we used to estimate temperature, metallicity and surface gravity from the observed colours is described in detail in appendix C, available online. We treated in this way all the stars in Table 2, seven of these land outside our grid when the appropriate gravity is assumed. In Fig. 12 we show the comparison between the spectroscopic [Fe/H] and the photometric metallicity estimates obtained from the above procedure, making use of Gaia parallaxes and photometry (filled symbols), and using only APASS photometry and no parallaxes (open symbols). It is clear that the use of the Gaia parallaxes improves considerably the photometric metallicity estimates because it allows to break the degeneracy between surface gravity and metallicity in the colours. If we select only the stars with the metallicity estimates that are closer to the spectroscopic ones ($|[{\rm Fe/H}]_{\rm spec} - [{\rm M/H}]_{\rm phot}| < 0.5$) we compute a linear rergession with an r.m.s. value of only 0.15 dex. The results of applying this "calibration" to all the data points is shown in the upper panel of Fig. 12. While there remain some clear outliers, most stars have a photometric metallicity estimate that is fully compatible, within errors, with the spectroscopic estimates. This gives us confidence that these photometric metallicity estimates can be used to select metal-poor stars for follow-up spectroscopy, but also for statistical studies (e.g. metallicity distribution functions) for large samples of stars.

It is reassuring to note that effective temperatures and surface gravities determined with this method are very close to what estimated making use of isochrones.

7 CONCLUSIONS.

To probe the effectiveness of Pristine (Starkenburg et al. 2017) in selecting metal-poor stars at its bright end we observed a sample of bright stars, selected as metal-ppor, with SOPHIE at the OHP 1.93 m telescope. We derived chemical abundances for 40 stars, 25 of which are confirmed metal-poor ([Fe/H]< -1.0) and eight are found to be very metal-poor ([Fe/H]< -2.0). No star proved to be with [Fe/H]< -3.0 although for nine stars the photometric metallicity estimate was lower than this.

Our selection effectiveness appears to be lower than what found by Youakim et al. (2017), although better than what achieved in Caffau et al. (2017). The use of APASS photometry has clearly improved over SDSS photometry, for the bright end, yet it is still sub-optimal. The calibration we implemented using Gaia photometry, parallaxes and Pristine photometry is very promising: the stellar parameters we derive are extremely close to the parameters derived from the isochrones and the metallicities are in good agreement with the [Fe/H] derived by the SOPHIE spectra. There are still exceptions of about 10% of the stars that are expected to be extremely metal-poor from our photometric calibration and in fact happen to be either metal-rich or only slightly metal-poor.

In few cases the isochrones used to derive the stellar parameters are too young for the expected ages of metal-poor stars. These stars can be blue stragglers or stars evolved from blue stragglers, but in principle the Galaxy could host a young, relatively metal-poor population, probably accreted from a satellite galaxy. The latter hypothesis seems however unlikely if the stars are α-rich. Age and metallicity estimates of larger samples of stars should allow to de-

[6] http://wwwuser.oats.inaf.it/castelli/grids.html

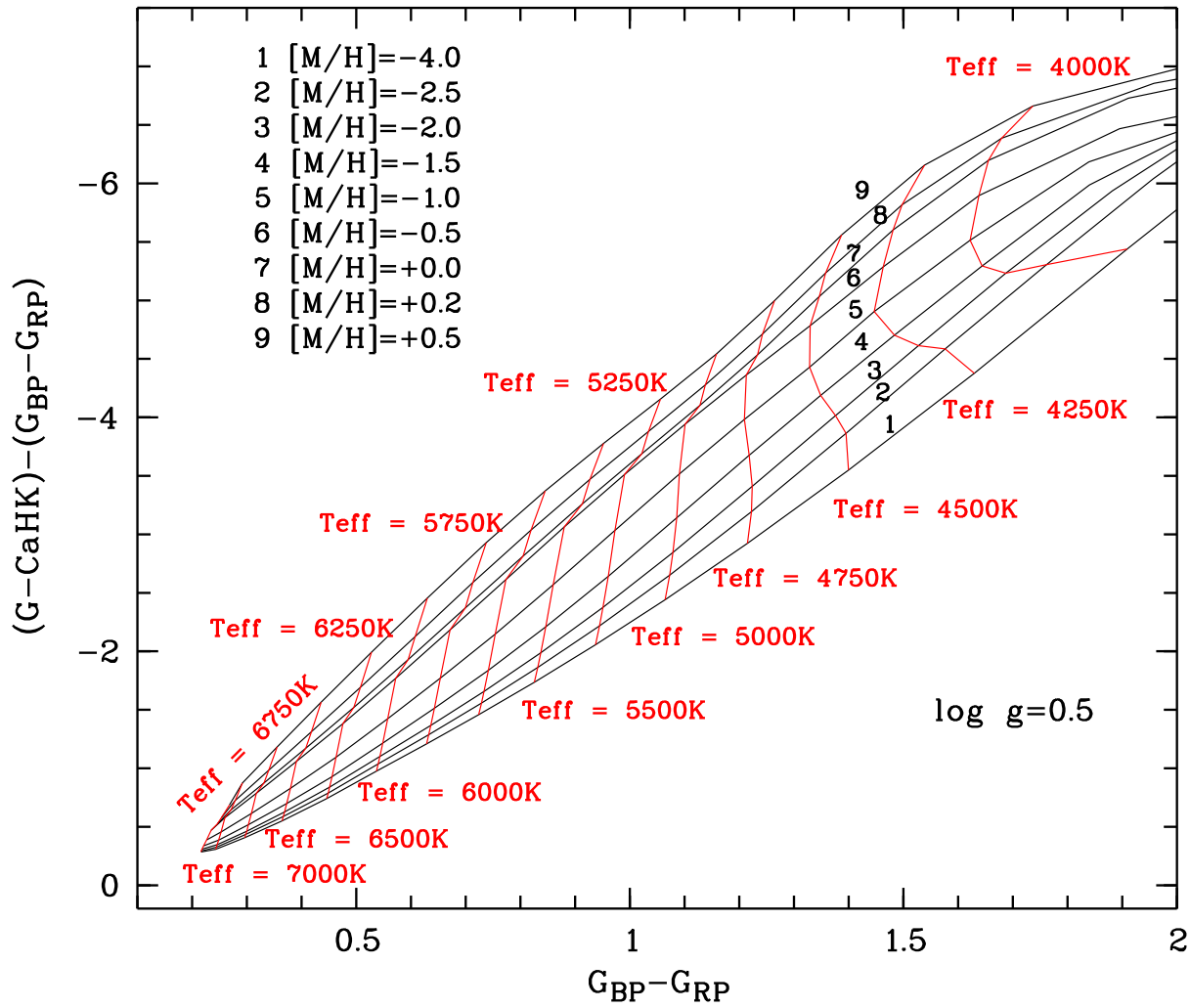

Figure 11. The theoretical colour-colour plane $(G_{BP} - G_{RP})$, $[(G - CaHK) - (G_{BP} - G_{RP})]$ for a fixed surface gravity $\log g = 0.5$. Lines of constant metallicity are shown in black and those of constant $T_{\rm eff}$ in red.

cide if the fraction of these "young metal-poor" stars is compatible with all of them being blue stragglers. Mass-estimates, for example for binary systems, should allow to establish if the stars are indeed blue stragglers. Better quality spectra should be able to either measure or put a stringent upper limit on their Li abundance. Blue stragglers are not expected to have any Li (see e.g. Pritchet & Glaspey 1991; Glaspey et al. 1994; Carney et al. 2005). Ryan et al. (2001) and Ryan et al. (2002) suggested a connection between Ultra-Li-depleted Halo Stars (stars for which no Li is measurable) and blue stragglers, suggesting that they are blue-stragglers-to-be. Recently, thanks to the Gaia DR2 parallaxes Bonifacio et al. (2019) showed that three out of the four stars studied by Ryan et al. (2001) are indeed canonical blue stragglers, rather than blue-stragglers-to-be.

One of the stars (Pristine_180.0750+16.3239) has a very high Li abundance. Unfortunately, the relatively low signal-to-noise ratio does not allow us to make any assessment on the ^{6}Li contribution to the feature.

One star, Pristine_212.2541+11.8045 shows an enhancement in Mg, but not in Ca or Ti. The line-to-line scatter is large, surely due to a poor signal-to-noise ratio (< 7 at 520 nm).

The astrometric data of Gaia allowed us to compute Galactic orbits for all the stars for which we could derive chemical abundances. In Sect.5.1 we classified these orbits making a minimum of assumptions. It is suggestive that a classification that is only based on the orbital parameters, translates into very clear abundance patterns.

We tentatively identify our "Halo" sample with the classical "outer halo" (Zinn 1985; Carollo et al. 2007, 2010). We are not in the position to discriminate wether these stars have been formed *in situ* or if they have been accreted. The Gaia data have permitted to unveil a massive accretion event that together with the thick disc should dominate the metal-poor populations in the Solar vicinity (Belokurov et al. 2018; Haywood et al. 2016; Helmi et al. 2018). In particular Haywood et al. (2016) separated the stars into two sequences that they call "Blue Sequence" and "Red Sequence". Gallart et al. (2019) argue that the "Red sequence" is composed by halo stars formed *in situ*, while Haywood et al. (2016) interpret it as being dominated by the thick disc. In appendix B,available online, we show in Fig. B1

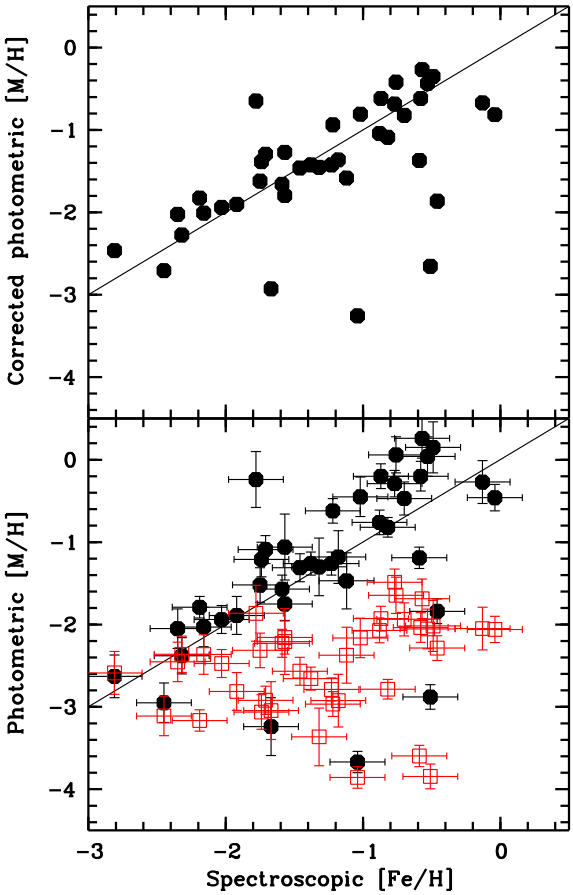

Figure 12. Comparison of the spectroscopic [Fe/H] with the photometric metallicity estimates. Lower panel: the estimate derived combining the Gaia data with the Pristine photometry, as described in the text as filled black hexagons, the estimate derived from APASS photometry and no estimate on gravities as open red squares. The line is the one-to-one relation, to guide the eye. Upper panel: the photometric metallicities as corrected with the linear fit described in the text.

that our sample belongs almost exclusively to the "Blue Sequence", this is hardly surprising since the sample was selected to search for metal-poor stars. Our "Halo" sample has very distinct chemical and kinematical properties, it may, nevertheless, be a mixture of stars formed *in situ* and stars accreted by one or several satellites. Haywood et al. (2016) argue that the stars that come from the single massive accretion event should be identified with the "low α" halo stars highlighted by Nissen & Schuster (2010), at [Fe/H]< -1.1, that form a unique sequence with the "high α" stars at higher metallicity. Both our "Halo" and our "Thick" sample do not contain any of "low α stars lke in Nissen & Schuster (2010).

We tentatively identify our "Thin" sample as "thin disc". With respect to other samples of thin disc stars that have been presented in the literature, our sample spans a larger range both in metalliicty and apocentric distance. The metallicity distribution of our sample is however heavily biased towards lower metallicity and it should not be used to infer information on the metallicity distribution of the disc. However, we think it is totally unbiased towards apocentric distances.

We tentatively identify the "Thick" class as thick disc. With respect to other kinematical definitions of the thick disc our "Thick" sample contains stars that are in very slow rotation or even in retrograde rotation, some stars have very small excursions from the Galactic plane. With respect to age the "Thick" class is predominantly old (age ≥ 8 Gyr), but not exclusively old. Besides the two suspect Blue Stragglers Pristine_183.4550+17.0927 and Pristine_206.9304+11.8894, we find Pristine_180.8994+16.3260 with an estimated age of 5.5 Gyr and Pristine_206.8050+00.7423 with an age estimate of 7.5 Gyr. As discussed above these may also be Blue Stragglers, or accreted from satellite galaxies. Probably the most surprising thing is that the "Thick" class, that contains considerable diversity in terms of kinematics and age, and covers a wide range of metallicities, from nearly solar to -2.5, shows a uniform distribution of [α/Fe] ≈ 0.39. If the "Thick" sample were just picked at random among diverse population, we would not expect such a chemical homogeneity. If a thick disc is formed by heating an old disc through satellite accretion events, we do expect a few retrograde or very slowly rotating orbits (see e.g. Jean-Baptiste et al. 2017). By looking at the kinematical diagrams Fig. A1 and Fig. A2 we may conclude that the "Thick" class may be interpreted either as a thick disc or as made dominantly by accreted stars from one or at most a few accretion events. If it were so, then the accreted galaxies should cover a wide range in metallicity, like the Sgr dSph (e.g. Bonifacio et al. 2004; Mucciarelli et al. 2017), and a sustained star formation rate that would produce high [α/Fe] ratios even at high metallicities. Both these facts suggest a rather massive galaxy, perhaps similar to Sgr dSph, with a mass of $10^8 M_\odot$, or larger.

ACKNOWLEDGEMENTS

We acknowledge support from the Agence National de la Recherche (ANR), through contract N. 183787. We are grateful to the Programme National des Galaxies et Cosmologie of the Institut National des Sciences de l'Univers of CNRS, for allocating the SOPHIE time used to acquire the data and for financial support. The authors thank the International Space Science Institute, Berne, Switzerland for providing financial support and meeting facilities to the international team "Pristine". FS and NFM gratefully acknowledge funding from CNRS/INSU through the Programme National Galaxies et Cosmologie and through the CNRS grant PICS07708. FS thanks the Initiative dExcellence IdEx from the University of Strasbourg and the Programme Doctoral International PDI for funding his PhD. This work has been published under the framework of the IdEx Unistra and benefits from a funding from the state managed by the French National Research Agency (ANR) as part of the investments for the future program. This research made use of the GravPot16 software, a community-developed core under the git version-control system on GitHub. This work has made use of data from the European Space Agency (ESA) mission *Gaia* (https://www.cosmos.esa.int/gaia), processed by the *Gaia* Data Processing and Analysis Consortium (DPAC, https://www.cosmos.esa.int/web/gaia/dpac/consortium). Funding for the DPAC has been provided by national institutions, in particular the institutions participating in the *Gaia* Multilateral Agreement.

REFERENCES

Allende Prieto C., Rebolo R., García López R. J., Serra-Ricart M., Beers T. C., Rossi S., Bonifacio P., Molaro P., 2000, AJ, 120, 1516

Amarsi A. M., Lind K., Asplund M., Barklem P. S., Collet R., 2016, MNRAS, 463, 1518

Anthony-Twarog B. J., Twarog B. A., 1998, AJ, 116, 1922

Anthony-Twarog B. J., Laird J. B., Payne D., Twarog B. A., 1991, AJ, 101, 1902

Anthony-Twarog B. J., Sarajedini A., Twarog B. A., Beers T. C., 2000, AJ, 119, 2882

Arenou F., et al., 2018a, A&A, 616, A17

Arenou F., et al., 2018b, A&A, 616, A17

Baade W., 1944, ApJ, 100, 137

Bailer-Jones C. A. L., 2015, PASP, 127, 994

Beers T. C., Preston G. W., Shectman S. A., 1985, AJ, 90, 2089

Beers T. C., Preston G. W., Shectman S. A., 1992, AJ, 103, 1987

Belokurov V., Irwin M. J., Koposov S. E., Evans N. W., Gonzalez-Solares E., Metcalfe N., Shanks T., 2014, MNRAS, 441, 2124

Belokurov V., Erkal D., Evans N. W., Koposov S. E., Deason A. J., 2018, MNRAS, 478, 611

Bensby T., Lind K., 2018, A&A, 615, A151

Bidelman W. P., MacConnell D. J., 1973, AJ, 78, 687

Binney J., 2012, MNRAS, 426, 1324

Bland-Hawthorn J., Gerhard O., 2016, ARA&A, 54, 529

Bond H. E., 1980, ApJS, 44, 517

Bonifacio P., Sbordone L., Marconi G., Pasquini L., Hill V., 2004, A&A, 414, 503

Bonifacio P., et al., 2007, A&A, 462, 851

Bonifacio P., Caffau E., Zaggia S., François P., Sbordone L., Andrievsky S. M., Korotin S. A., 2015, A&A, 579, L6

Bonifacio P., et al., 2018a, A&A, 611, A68

Bonifacio P., et al., 2018b, A&A, 612, A65

Bonifacio P., Caffau E., Spite M., Spite F., 2019, Research Notes of the American Astronomical Society, 3, 64

Bouchy F., Sophie Team 2006, in Arnold L., Bouchy F., Moutou C., eds, Tenth Anniversary of 51 Peg-b: Status of and prospects for hot Jupiter studies. pp 319–325

Bovy J., 2015, The Astrophysical Journal Supplement Series, 216, 29

Bressan A., Marigo P., Girardi L., Salasnich B., Dal Cero C., Rubele S., Nanni A., 2012, MNRAS, 427, 127

Burkardt J., 2009, TABLE_DELAUNAY, https://people.sc.fsu.edu/~jburkardt

Caffau E., Ludwig H.-G., Steffen M., Freytag B., Bonifacio P., 2011, Sol. Phys., 268, 255

Caffau E., et al., 2017, Astronomische Nachrichten, 338, 686

Cain M., et al., 2018, ApJ, 864, 43

Carney B. W., Latham D. W., Laird J. B., 2005, AJ, 129, 466

Carollo D., et al., 2007, Nature, 450, 1020

Carollo D., et al., 2010, ApJ, 712, 692

Casagrande L., Wolf C., Mackey A. D., Nordlander T., Yong D., Bessell M., 2019, MNRAS, 482, 2770

Castelli F., Kurucz R. L., 2003, in Piskunov N., Weiss W. W., Gray D. F., eds, IAU Symposium Vol. 210, Modelling of Stellar Atmospheres. p. A20

Castelli F., Kurucz R. L., 2004, ArXiv Astrophysics e-prints,

Cayrel R., et al., 2004, A&A, 416, 1117

Chamberlain J. W., Aller L. H., 1951, ApJ, 114, 52

Chiappini C., et al., 2015, A&A, 576, L12

Christlieb N., 2003, in Schielicke R. E., ed., Reviews in Modern Astronomy Vol. 16, Reviews in Modern Astronomy. p. 191 (arXiv:astro-ph/0308016), doi:10.1002/9783527617647.ch8

Delaunay B., 1934, Bulletin de l'Académie des Sciences de l'URSS, Classe des sciences mathématiques et naturelles, 6, 793

Evans D. W., et al., 2018, A&A, 616, A4

Fernández-Trincado J. G., 2019, ApJS, in prep.

Fuhrmann K., Bernkopf J., 1999, A&A, 347, 897

Gaia Collaboration et al., 2016, A&A, 595, A1

Gaia Collaboration et al., 2018, A&A, 616, A1

Gallart C., Bernard E. J., Brook C. B., Ruiz-Lara T., Cassisi S., Hill V., Monelli M., 2019, arXiv e-prints,

Glaspey J. W., Pritchet C. J., Stetson P. B., 1994, AJ, 108, 271

González Hernández J. I., Bonifacio P., 2009, A&A, 497, 497

Green G. M., et al., 2018a, MNRAS, 478, 651

Green G. M., et al., 2018b, MNRAS, 478, 651

Harutyunyan G., Steffen M., Mott A., Caffau E., Israelian G., González Hernández J. I., Strassmeier K. G., 2018, preprint, (arXiv:1807.04089)

Haywood M., Di Matteo P., Lehnert M. D., Katz D., Gómez A., 2013, A&A, 560, A109

Haywood M., Lehnert M. D., Di Matteo P., Snaith O., Schultheis M., Katz D., Gómez A., 2016, A&A, 589, A66

Helmi A., Babusiaux C., Koppelman H. H., Massari D., Veljanoski J., Brown A. G. A., 2018, Nature, 563, 85

Henden A., Munari U., 2014, Contributions of the Astronomical Observatory Skalnate Pleso, 43, 518

Henden A. A., Welch D. L., Terrell D., Levine S. E., 2009, in American Astronomical Society Meeting Abstracts #214. p. 669

Henden A. A., Levine S., Terrell D., Welch D. L., 2015, in American Astronomical Society Meeting Abstracts #225. p. 336.16

Henden A. A., Levine S., Terrell D., Welch D. L., Munari U., Kloppenborg B. K., 2018, in American Astronomical Society Meeting Abstracts #232. p. 223.06

Hoeg E., et al., 1997, A&A, 323, L57

Jean-Baptiste I., Di Matteo P., Haywood M., Gómez A., Montuori M., Combes F., Semelin B., 2017, A&A, 604, A106

Keenan P. C., 1942, ApJ, 96, 101

Keenan P. O., Morgan W. W., Münch G., 1948, AJ, 53, 194

Keller S. C., et al., 2007, Publ. Astron. Soc. Australia, 24, 1

Kirby E. N., Simon J. D., Cohen J. G., 2015, ApJ, 810, 56

Korotin S. A., Andrievsky S. M., Hansen C. J., Caffau E., Bonifacio P., Spite M., Spite F., François P., 2015, A&A, 581, A70

Kurucz R., 1993, Solar Abundance Model Atmospheres for 0,1,2,4,8 km/s. Kurucz CD-ROM No. 19. Cambridge, Mass.: Smithsonian Astrophysical Observatory, 1993., 19

Lindblad B., 1922, ApJ, 55

Lodders K., Palme H., Gail H.-P., 2009, Landolt Börnstein, p. 712

Luck R. E., Bond H. E., 1981, ApJ, 244, 919

Luri X., et al., 2018, A&A, 616, A9

Marigo P., et al., 2017, ApJ, 835, 77

Martig M., et al., 2015, MNRAS, 451, 2230

Masseron T., et al., 2014, A&A, 571, A47

Meléndez J., Placco V. M., Tucci-Maia M., Ramírez I., Li T. S., Perez G., 2016, A&A, 585, L5

Mott A., Steffen M., Caffau E., Spada F., Strassmeier K. G., 2017, A&A, 604, A44

Mucciarelli A., Bellazzini M., Ibata R., Romano D., Chapman S. C., Monaco L., 2017, A&A, 605, A46

Navarro J. F., Frenk C. S., White S. D. M., 1997, ApJ, 490, 493

Nissen P. E., Schuster W. J., 2010, A&A, 511, L10

Nissen P. E., Gustafsson B., Edvardsson B., Gilmore G., 1994, A&A, 285, 440

Norris J., Bessell M. S., Pickles A. J., 1985, ApJS, 58, 463

Oort J. H., 1926a, PhD thesis, Publications of the Kapteyn Astronomical Laboratory Groningen, vol. 40, pp.1-75

Oort J. H., 1926b, The Observatory, 49, 302

Placco V. M., et al., 2019, ApJ, 870, 122

Popper D. M., 1947, ApJ, 105, 204

Pritchet C. J., Glaspey J. W., 1991, ApJ, 373, 105

Ryan S. G., Beers T. C., Kajino T., Rosolankova K., 2001, ApJ, 547, 231

Ryan S. G., Gregory S. G., Kolb U., Beers T. C., Kajino T., 2002, ApJ, 571, 501
Salvadori S., Ferrara A., Schneider R., Scannapieco E., Kawata D., 2010, MNRAS, 401, L5
Sartoretti P., et al., 2018, A&A, 616, A6
Sbordone L., Caffau E., Bonifacio P., Duffau S., 2014, A&A, 564, A109
Schlaufman K. C., Casey A. R., 2014, ApJ, 797, 13
Schlaufman K. C., Thompson I. B., Casey A. R., 2018, ApJ, 867, 98
Schönrich R., Binney J., Dehnen W., 2010, MNRAS, 403, 1829
Schuster W. J., Nissen P. E., Parrao L., Beers T. C., Overgaard L. P., 1996, A&AS, 117, 317
Schuster W. J., Parrao L., Franco A., Beers T. C., Nissen P. E., 1999, Ap&SS, 265, 183
Schuster W. J., Beers T. C., Michel R., Nissen P. E., García G., 2004, A&A, 422, 527
Schwarzschild M., Spitzer Jr. L., Wildt R., 1951, ApJ, 114, 398
Sestito F., et al., 2019, MNRAS, 484, 2166
Spite M., Spite F., 1982, Nature, 297, 483
Spite M., Bonifacio P., Spite F., Caffau E., Sbordone L., Gallagher A J., 2019, A&A, submitted
Starkenburg E., et al., 2017, MNRAS, 471, 2587
Steffen M., Caffau E., Ludwig H.-G., 2013, Memorie della Società Astronomica Italiana Supplementi, 24, 37
Twarog B. A., Anthony-Twarog B. J., 1995, AJ, 109, 2828
Voggel K., Hilker M., Baumgardt H., Collins M. L. M., Grebel E. K., Husemann B., Richtler T., Frank M. J., 2016, MNRAS, 460, 3384
York D. G., et al., 2000, AJ, 120, 1579
Youakim K., et al., 2017, MNRAS, 472, 2963
Zinn R., 1985, ApJ, 293, 424

APPENDIX A: KINEMATIC PROPERTIES

In this appendix we provide in Table,A1 and A2 the kinematic properties of the sample of stars we have analysed and some of the quantities derived from their Galactic orbits. The space velocities (U, V, W) are with respect to the Local Standard of Rest, U is positive towards the Galactic anti-centre, V in the direction of the Galactic rotation and W is perpendicular to the Galactic plane, positive in the northern Galactic hemisphere. We list also the mean specific angular momentum (angular momentum per unit mass) for the stars along their orbits, in units of $\mathrm{kpc}\times\mathrm{km\,s^{-1}}$. In Fig. A1 we provide the Toomre diagram for the sample of stars and in Fig. A2 the diagram of mean specific angular momentum versus the energy and J_z action for our sample.

APPENDIX B: EVOLUTIONARY DIAGRAM

In this appendix we show, in Fig, B1, the log ($T_{\rm eff}$) - log g diagram for our stars. This is morphologically equivalent to a colour-magnitude diagram. We recall that in our case the surface gravities have been derived from the G absolute magnitudes and the effective temperatures from the $G_{BP}-G_{RP}$ colours. As a reference we show on the diagram two PARSEC isochrones (Bressan et al. 2012; Marigo et al. 2017) of 11.5 Gyr and metalliciy -0.5 and -1.5. The isochrone of metallicity -0.5 is the one used by Haywood et al. (2016) to separate the "Blue Sequence", from the "Red Sequence" stars. The plot shows that all of our stars, except, perhaps two, belong to the "Blue Sequence".

APPENDIX C: TRIANGULATION AND INTERPOLATION IN THE COLOUR-COLOUR PLANE

In what follows, all colours are assumed to be corrected for reddening. We take advantage of the Gaia parallaxes also to estimate the surface gravity of the star via the Stefan-Boltzman equation (see e.g. equation (1) of Nissen et al. 1994). To do so, however, we need an estimate of the mass of the star, of its effective temperature and its bolometric magnitude. The mass is not very important, the old stars that are the main targets of the Pristine survey have masses in the range 0.7 to 0.9 $\mathrm{M}\odot$, this implies an uncertainty of only 0.1 dex in the surface gravity, therefore we can safely assume a mass of 0.8 $\mathrm{M}\odot$. The G band is very wide and the bolometric correction is very small, however we need to know the star's parameters in order to have the bolometric correction.

Once a first guess of the surface gravity is made we can interpolate in the theoretical colour-colour grid and determine the grid for this gravity. At this point, from the mathematical point of view, the problem is to determine the values of $T_{\rm eff}$ and metallicity for the observed values of $(G_{BP}-G_{RP})$ and $(G-CaHK)-(G_{BP}-G_{RP})$. $T_{\rm eff}$ and metallicity are assumed to be continuous functions of the two colours and their values are known only for a finite set of points in the colour-colour plane. These points are not on a regular grid in the colour-colour plane. Our approach is to divide the plane using a set of non-overlapping triangles and we decided to use the Delaunay triangulation (Delaunay 1934). This has the property that none of the points that define the triangulation is internal to the circumcircle of any triangle. To compute the triangulation we used the Fortran 90 code of Burkardt (2009), slightly modified to be used by our own code as a subroutine. To establish in which triangle lies our point we compute barycentric coordinates of the observed point for each triangle, when all three coordinates are ≥ 0 then the point is inside the triangle. At this point we could simply proceed to estimate the values of $T_{\rm eff}$ and metallicity at the observed point by barycentric interpolation[7]. This however could be sub-optimal if the three vertexes of the triangle lie on three different iso-metallicity line (see Fig. C1). The optimal interpolation is for a triangle, containing the observed point, that has a side along an iso-metallicity line. It is however trivial to find such a triangle, starting from the Delaunay triangle whose vertexes lie on three iso-metallicity lines. It is sufficient to consider the intersection of the median iso-metallicity line with the segment uniting the two other vertexes of the Delaunay triangle. Then consider the two triangles that have as one side the segment between this point and the original vertex at the median metallicity and as third vertex one of the two other vertexes of the Delaunay triangle. The observed point is necessarily internal to one of these two triangles and again we use barycentric coordinates to determine which of the two. Refer to Fig. C1 to picture the situation.

In summary we adopted the following iterative procedure:

(i) if $(G_{BP}-G_{RP})\leq 0.8$ assume log g = 4.0, else assume log g = 2.5;
(ii) assume a metallicity –1.0;
(iii) interpolate in the theoretical colours to find the $T_{\rm eff}$ and bolometric correction that correspond to this $(G_{BP}-G_{RP})$;
(iv) compute the bolometric magnitude;
(v) use the Stefan-Boltzman equation, to estimate log g;
(vi) with the new log g go to point (iii) and iterate until the variation in log g is less than 0.1 dex;
(vii) with the current guess of log g interpolate in the theoretical colours to get the points in the colour-colour plane corresponding to this log g;
(viii) compute a Delaunay triangulation for this data set;
(ix) for each triangle compute the barycentric coordinates of the observed point;
(x) if the three barycentric coordinates are all positive (or zero) then the point is inside that triangle;
(xi) if the point is not in any of the triangles, set a warning condition exit the loop and process the next star;
(xii) check if the triangle lies between two iso-metallicity lines, if so proceed to point (xiv), else;
(xiii) refine the triangle identifying the non-Delaunay triangle that contains the point and lies between two subsequent iso-metallicity lines;
(xiv) use the barycentric coordinates to obtain the barycentric interpolated value of $T_{\rm eff}$ and metallicity;

[7] Once we know the three vertexes of the triangle, points P_1, P_2, P_3 we also now the value of $T_{\rm eff}(T_1, T_2, T_3)$ and metallicity at each point. If b_1, b_2, b_2 are the barycentric coordinates of a point inside the triangle, then the value of $T_{\rm eff}$ at that point can be estimated as $b_1T_1 + b_2T_2 + b_3T_3$ and likewise for metallicity.

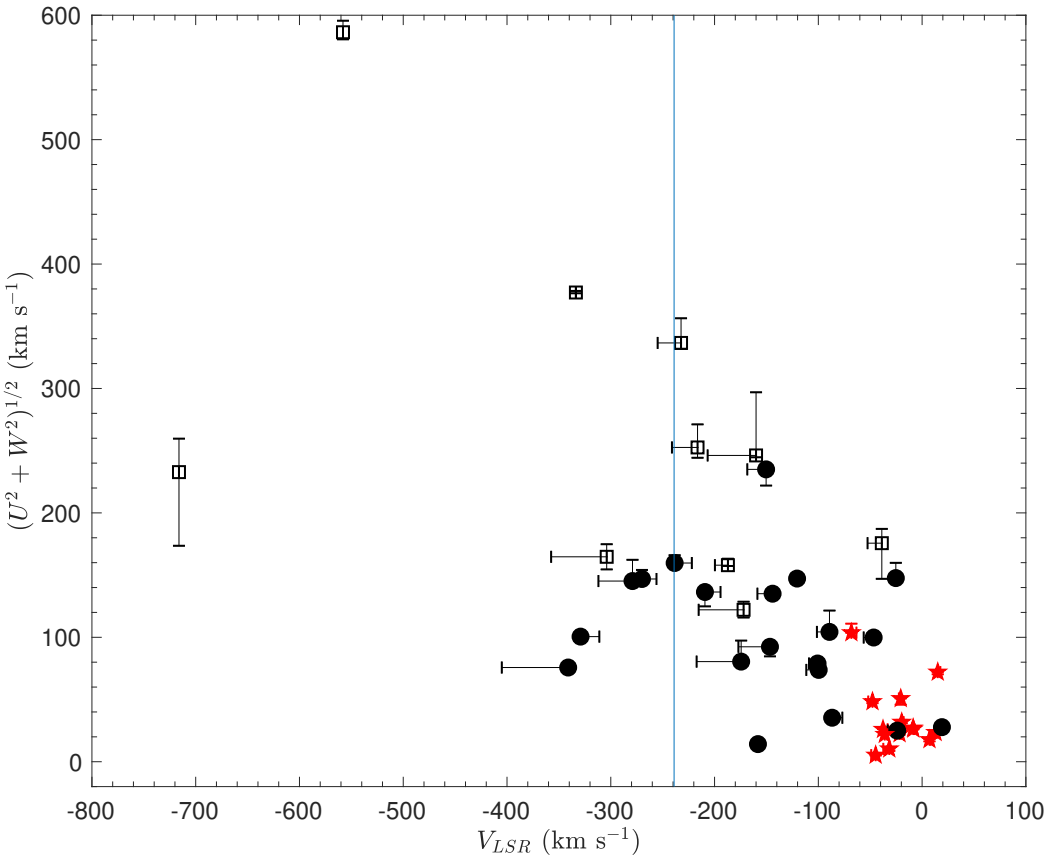

Figure A1. The Toomre diagram for our stars. Black dots are stars classified as "Thick", red stars are stars classified as "Thin" and open squares are stars classified as "Halo". 298.

(xv) with this new metallicity and the current gravity interpolate the theoretical colour $G_{BP} - G_{RP}$ for all effective temperatures;

(xvi) determine a new effective temperature by a spline interplation in this curve for the observed $G_{BP}-G_{RP}$ colour;

(xvii) with the new $T_{\rm eff}$compute a new bolometric correction and log g;

(xviii) chek the variation of $T_{\rm eff}$ and log g with respect to the previous estimates is "small enough" [8], if not go back to step (iii).

This paper has been typeset from a TEX/LATEX file prepared by the author.

[8] We used 50 K for $T_{\rm eff}$ and 0.1 dex for log g.

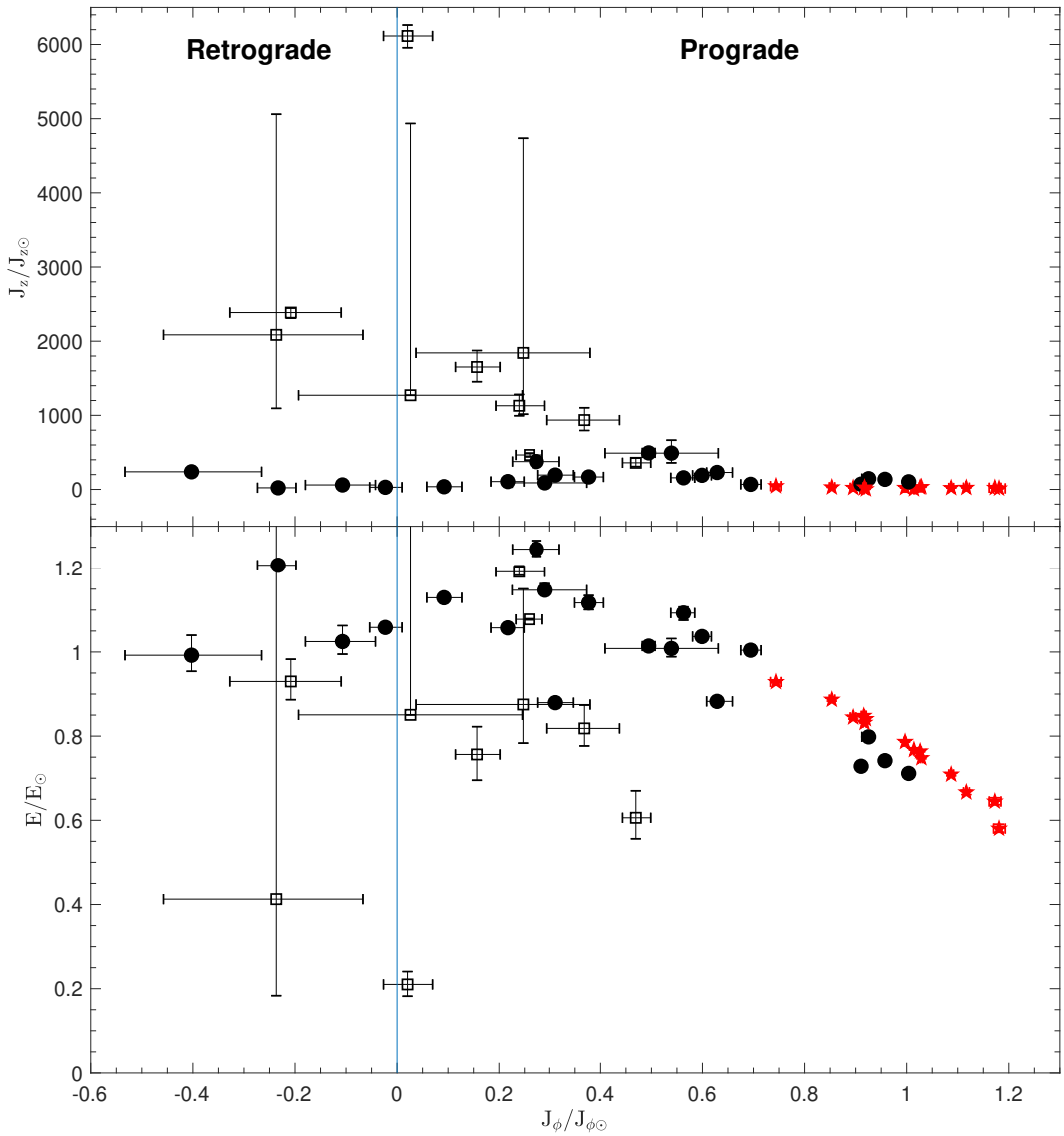

Figure A2. The specific energy versus rotational action J_ϕ (also knonw as specific angular momentum L_z) diagram for our stars (lower panel) and the J_z action (as defined in equation 6 of Binney 2012) versus rotational action (upper panel). All the quantites are normalized to the solar value. The symbols are the same as in Fig.A1.

Table A1. Inferred orbital parameters of the stars in the sample. The velocity (U,V,W) in the heliocentric frame, the apocentre and pericentre distances in the galactocentric frame are listed.

Target	U ($km\,s^{-1}$)	V ($km\,s^{-1}$)	W ($km\,s^{-1}$)	Apo (kpc)	Peri (kpc)
Pristine_110.0459+43.0522	$33.9^{+1.0}_{-8.2}$	-341^{+1}_{-64}	$-67.7^{+2.6}_{-2.7}$	$10.6^{+0.2}_{-0.2}$	$2.4^{+0.9}_{-1.0}$
Pristine_110.4208+40.8947	8^{+1}_{-13}	-304^{+1}_{-54}	-164^{+10}_{-10}	$9.9^{+0.1}_{-0.1}$	$4.1^{+1.6}_{-1.1}$
Pristine_111.5919+44.0179	$38.8^{+1.0}_{-1.5}$	$-47.8^{+1.0}_{-4.1}$	$-28.8^{+0.4}_{-0.4}$	$10.1^{+0.1}_{-0.1}$	$7.1^{+0.1}_{-0.1}$
Pristine_112.0456+43.9914	$-24.4^{+1.0}_{-2.2}$	$-37.7^{+4.4}_{-1.0}$	$-9.0^{+0.9}_{-1.0}$	$10.0^{+0.1}_{-0.1}$	$8.9^{+0.1}_{-0.1}$
Pristine_112.3237+44.2279	$11.9^{+1.0}_{-1.7}$	$13.0^{+1.3}_{-1.0}$	$20.3^{+1.0}_{-1.0}$	$14.4^{+0.2}_{-0.2}$	$8.4^{+0.1}_{-0.1}$
Pristine_112.5667+45.9455	$70.6^{+1.0}_{-1.8}$	$15.1^{+2.5}_{-1.0}$	$-14.5^{+0.7}_{-0.8}$	$18.0^{+0.4}_{-0.3}$	$8.0^{+0.1}_{-0.1}$
Pristine_112.6119+45.7784	$-26.2^{+1.4}_{-1.0}$	$-8.4^{+0.9}_{-1.0}$	$1.6^{+0.4}_{-0.4}$	$11.2^{+0.1}_{-0.1}$	$8.3^{+0.1}_{-0.1}$
Pristine_113.0244+45.6965	$26.2^{+2.0}_{-1.0}$	$-19.6^{+1.8}_{-1.0}$	$18.0^{+1.4}_{-1.4}$	$11.7^{+0.1}_{-0.1}$	$8.4^{+0.1}_{-0.1}$
Pristine_113.4132+41.9324	$-2.8^{+1.4}_{-1.0}$	$-44.7^{+1.0}_{-4.3}$	$4.5^{+0.3}_{-0.4}$	$9.0^{+0.1}_{-0.1}$	$8.2^{+0.1}_{-0.1}$
Pristine_113.4275+45.6423	$8.6^{+1.0}_{-1.9}$	$-31.6^{+1.0}_{-5.7}$	$-5.6^{+0.4}_{-0.4}$	$10.5^{+0.1}_{-0.1}$	$9.1^{+0.1}_{-0.1}$
Pristine_113.6421+45.4681	$-14.1^{+1.0}_{-1.7}$	$7.1^{+1.2}_{-1.0}$	$-10.9^{+0.9}_{-1.0}$	$14.6^{+0.3}_{-0.2}$	$9.1^{+0.1}_{-0.1}$
Pristine_113.6744+45.8738	$-86.6^{+1.7}_{-1.0}$	$-46.7^{+1.0}_{-9.6}$	$49.6^{+0.7}_{-0.7}$	$12.9^{+0.1}_{-0.1}$	$7.2^{+0.1}_{-0.1}$
Pristine_113.7050+45.5860	$21.7^{+1.0}_{-1.5}$	$-8.6^{+1.0}_{-0.7}$	$-16.1^{+0.3}_{-0.3}$	$12.6^{+0.1}_{-0.1}$	$8.7^{+0.1}_{-0.1}$
Pristine_180.0750+16.3239	$17.1^{+1.0}_{-1.0}$	$-21.7^{+1.5}_{-1.0}$	$-14.7^{+0.5}_{-0.5}$	$9.8^{+0.1}_{-0.1}$	$7.6^{+0.1}_{-0.1}$
Pristine_180.8898+15.6500	$136.0^{+18.0}_{-1.0}$	$-279.0^{+1.0}_{-33.0}$	$-49.9^{+3.5}_{-4.3}$	$11.0^{+0.6}_{-0.4}$	$0.7^{+0.3}_{-0.3}$
Pristine_180.8994+16.3260	$9.2^{+4.2}_{-1.0}$	$-24.0^{+1.0}_{-9.1}$	$-23.2^{+0.9}_{-0.8}$	$10.7^{+0.1}_{-0.1}$	$7.8^{+0.1}_{-0.1}$
Pristine_181.4437+13.4888	$5.9^{+1.0}_{-0.6}$	$-100.7^{+1.0}_{-8.3}$	$-78.7^{+1.3}_{-1.6}$	$8.2^{+0.1}_{-0.1}$	$4.5^{+0.2}_{-0.2}$
Pristine_182.2972+13.1228	131^{+1}_{-12}	-209^{+15}_{-1}	$39.7^{+2.1}_{-2.4}$	$10.2^{+0.2}_{-0.2}$	$1.1^{+0.2}_{-0.2}$
Pristine_183.1390+16.1839	$-12.4^{+1.0}_{-1.8}$	$-86.7^{+9.9}_{-1.0}$	$-33.1^{+1.3}_{-1.5}$	$8.1^{+0.1}_{-0.1}$	$5.4^{+0.3}_{-0.2}$
Pristine_183.4550+17.0927	101^{+18}_{-1}	-89^{+1}_{-12}	$26.1^{+1.2}_{-1.1}$	$11.6^{+0.3}_{-0.3}$	$4.1^{+0.3}_{-0.1}$
Pristine_185.5596+15.5893	-144^{+13}_{-1}	$-25.3^{+1.0}_{-1.7}$	$32.2^{+0.5}_{-0.5}$	$14.3^{+0.4}_{-0.4}$	$6.0^{+0.1}_{-0.1}$
Pristine_188.4543+15.1750	$-49.9^{+1.0}_{-5.0}$	$-20.6^{+1.0}_{-1.8}$	$9.2^{+0.5}_{-0.5}$	$10.1^{+0.1}_{-0.1}$	$7.5^{+0.1}_{-0.1}$
Pristine_191.9208+16.0031	$-12.7^{+1.0}_{-1.0}$	$-158.2^{+1.0}_{-1.0}$	$-6.3^{+3.6}_{-5.3}$	$8.5^{+0.5}_{-0.2}$	$4.4^{+0.9}_{-1.2}$
Pristine_192.4508+12.7922	$-103.2^{+7.3}_{-1.0}$	$-68.2^{+4.9}_{-1.0}$	$-9.7^{+0.5}_{-0.5}$	$9.7^{+0.1}_{-0.1}$	$5.3^{+0.1}_{-0.1}$
Pristine_193.5777+10.3945	$-124.4^{+6.5}_{-1.0}$	-187^{+1}_{-13}	$-97.4^{+1.2}_{-1.0}$	$9.2^{+0.1}_{-0.1}$	$1.9^{+0.2}_{-0.4}$
Pristine_195.1494+06.5655	226^{+29}_{-1}	-232^{+1}_{-23}	$249.3^{+6.4}_{-6.4}$	$40.7^{+2.7}_{-2.2}$	$5.9^{+0.1}_{-0.1}$
Pristine_198.3167+14.9688	$21.8^{+1.7}_{-1.0}$	$-36.0^{+2.5}_{-1.0}$	$2.2^{+0.6}_{-0.6}$	$9.1^{+0.1}_{-0.1}$	$7.1^{+0.1}_{-0.1}$
Pristine_206.8050+00.7423	77^{+17}_{-1}	-174^{+1}_{-43}	$-22.4^{+9.8}_{-8.2}$	$8.7^{+0.1}_{-0.1}$	$1.6^{+0.6}_{-0.4}$
Pristine_206.9304+11.8894	$146.9^{+7.3}_{-1.0}$	-270^{+14}_{-1}	$0.2^{+2.4}_{-2.1}$	$10.5^{+0.2}_{-0.2}$	$0.4^{+0.2}_{-0.1}$
Pristine_212.2541+11.4580	$23.2^{+1.0}_{-1.0}$	$-716.1^{+1.0}_{-1.0}$	-232^{+27}_{-59}	$11.1^{+102.6}_{-0.1}$	$2.4^{+3.1}_{-1.3}$
Pristine_213.1910+14.7927	$-376.8^{+1.0}_{-1.0}$	$-333.6^{+1.0}_{-1.0}$	15^{+32}_{-16}	$9.4^{+6.4}_{-0.1}$	$3.4^{+1.6}_{-0.2}$
Pristine_216.1506+14.1298	$-575.5^{+1.0}_{-1.0}$	$-558.1^{+1.0}_{-1.0}$	112^{+48}_{-30}	$36.2^{+182.9}_{-22.9}$	$3.0^{+5.5}_{-2.0}$
Pristine_219.0145+11.6057	$-26.4^{+1.0}_{-3.8}$	$19.1^{+3.4}_{-1.0}$	$8.7^{+1.0}_{-1.0}$	$13.7^{+0.3}_{-0.2}$	$7.4^{+0.1}_{-0.1}$
Pristine_232.8856+07.8678	$-29.5^{+3.9}_{-1.0}$	-100^{+1}_{-12}	$-67.7^{+0.6}_{-0.7}$	$7.5^{+0.1}_{-0.1}$	$4.3^{+0.2}_{-0.3}$
Pristine_234.0338+12.6370	$-95.6^{+1.0}_{-1.3}$	$-120.5^{+1.0}_{-5.6}$	$-111.9^{+0.7}_{-0.6}$	$8.9^{+0.1}_{-0.1}$	$3.8^{+0.1}_{-0.1}$
Pristine_235.0278+07.5059	$11.2^{+1.0}_{-7.6}$	-172^{+1}_{-43}	$121.6^{+6.6}_{-6.2}$	$6.5^{+0.1}_{-0.1}$	$2.8^{+0.3}_{-0.3}$
Pristine_235.0537+07.5988	$-100.5^{+1.0}_{-1.5}$	-329^{+18}_{-1}	$-4.0^{+3.2}_{-2.9}$	$8.2^{+0.1}_{-0.1}$	$1.2^{+0.3}_{-0.2}$
Pristine_236.4719+15.3328	$-158.6^{+6.3}_{-1.0}$	-238^{+17}_{-1}	$18.9^{+6.0}_{-6.2}$	$9.5^{+0.1}_{-0.1}$	$0.6^{+0.6}_{-0.1}$
Pristine_236.7635+05.4474	-233^{+1}_{-13}	-150^{+1}_{-18}	$-32.4^{+8.1}_{-8.1}$	$13.2^{+0.1}_{-0.1}$	$1.7^{+0.2}_{-0.2}$
Pristine_237.8581+07.1456	158^{+27}_{-1}	-216^{+1}_{-25}	-197^{+10}_{-11}	$15.5^{+1.9}_{-1.6}$	$2.1^{+0.2}_{-0.2}$
Pristine_238.2716+07.5917	$-91.8^{+1.0}_{-7.7}$	-147^{+1}_{-30}	$10.5^{+6.4}_{-6.4}$	$6.9^{+0.1}_{-0.1}$	$1.9^{+0.3}_{-0.2}$
Pristine_240.2908+07.9401	-117^{+1}_{-40}	-39^{+1}_{-14}	131^{+15}_{-13}	$13.7^{+1.6}_{-1.3}$	$2.8^{+0.4}_{-0.5}$
Pristine_241.1299+06.3632	$-119.9^{+1.3}_{-1.0}$	-144^{+1}_{-15}	$-62.2^{+2.6}_{-2.7}$	$8.6^{+0.1}_{-0.1}$	$2.3^{+0.2}_{-0.2}$
Pristine_246.4406+15.0900	243^{+51}_{-1}	-160^{+1}_{-47}	$-38.7^{+8.0}_{-9.5}$	$20.5^{+2.8}_{-1.8}$	$2.6^{+0.2}_{-0.2}$

Table A2. Inferred orbital parameters of the stars in the sample. The eccentricity $\epsilon = (r_{apo} - r_{peri})/(r_{apo} + r_{peri})$ of the orbit, the energy and the rotational, the radial and the vertical components of the action (J_ϕ, J_r, J_z), the maximum height z_{max}, and the kind of orbit are listed.

Target	ϵ	E ($\mathrm{km\,s^{-1}\,km\,s^{-1}}$)	J_ϕ ($\mathrm{kpc\,km\,s^{-1}}$)	J_r ($\mathrm{kpc\,km\,s^{-1}}$)	J_z ($\mathrm{kpc\,km\,s^{-1}}$)	z_{max} (kpc)	Orbit
Pristine_110.0459+43.0522	$0.623^{+0.133}_{-0.098}$	$-64442.4^{+3098.1}_{-2478.5}$	$-809.3^{+275.6}_{-261.8}$	$392.9^{+135.8}_{-107.5}$	$83.8^{+8.2}_{-9.9}$	$2.53^{+0.16}_{-0.19}$	Thick
Pristine_110.4208+40.8947	$0.407^{+0.116}_{-0.140}$	$-60390.7^{+3438.7}_{-2813.4}$	$-418.5^{+198.4}_{-240.2}$	$207.8^{+154.9}_{-112.2}$	$840.3^{+21.7}_{-26.4}$	$9.18^{+0.38}_{-0.57}$	Halo
Pristine_111.5919+44.0179	$0.175^{+0.002}_{-0.002}$	$-54848.0^{+203.6}_{-254.4}$	$1799.0^{+10.7}_{-11.9}$	$38.2^{+0.8}_{-0.8}$	$7.7^{+0.6}_{-0.5}$	$0.61^{+0.03}_{-0.02}$	Thin
Pristine_112.0456+43.9914	$0.061^{+0.002}_{-0.002}$	$-51076.8^{+56.6}_{-63.7}$	$2003.5^{+3.6}_{-4.0}$	$5.0^{+0.4}_{-0.3}$	$7.7^{+0.8}_{-0.7}$	$0.60^{+0.03}_{-0.03}$	Thin
Pristine_112.3237+44.2279	$0.264^{+0.005}_{-0.005}$	$-43283.1^{+349.7}_{-349.7}$	$2244.8^{+12.1}_{-11.3}$	$112.4^{+5.0}_{-4.4}$	$8.0^{+0.7}_{-0.7}$	$0.83^{+0.05}_{-0.05}$	Thin
Pristine_112.5667+45.9455	$0.383^{+0.006}_{-0.006}$	$-37690.1^{+664.4}_{-569.5}$	$2373.4^{+24.4}_{-21.7}$	$270.0^{+13.1}_{-11.6}$	$4.6^{+0.4}_{-0.3}$	$0.73^{+0.04}_{-0.03}$	Thin
Pristine_112.6119+45.7784	$0.149^{+0.002}_{-0.002}$	$-49831.8^{+35.0}_{-31.8}$	$2038.4^{+0.9}_{-0.8}$	$30.8^{+0.7}_{-0.6}$	$1.6^{+1.0}_{-1.0}$	$0.27^{+0.00}_{-0.01}$	Thin
Pristine_113.0244+45.6965	$0.163^{+0.001}_{-0.001}$	$-48562.0^{+132.8}_{-110.7}$	$2067.8^{+3.8}_{-3.4}$	$38.0^{+0.5}_{-0.5}$	$11.7^{+1.5}_{-1.3}$	$0.87^{+0.07}_{-0.06}$	Thin
Pristine_113.4132+41.9324	$0.047^{+0.008}_{-0.008}$	$-55087.1^{+212.3}_{-179.7}$	$1840.7^{+10.0}_{-10.0}$	$2.7^{+1.0}_{-0.8}$	$6.3^{+0.4}_{-0.5}$	$0.49^{+0.02}_{-0.02}$	Thin
Pristine_113.4275+45.6423	$0.071^{+0.008}_{-0.008}$	$-49603.9^{+84.6}_{-76.2}$	$2062.9^{+3.5}_{-3.0}$	$7.1^{+1.8}_{-1.6}$	$10.1^{+1.4}_{-1.4}$	$0.73^{+0.05}_{-0.06}$	Thin
Pristine_113.6421+45.4681	$0.233^{+0.004}_{-0.004}$	$-41866.8^{+580.4}_{-491.1}$	$2356.9^{+24.0}_{-22.1}$	$90.6^{+4.6}_{-3.8}$	$7.7^{+0.9}_{-0.8}$	$0.82^{+0.06}_{-0.06}$	Thin
Pristine_113.6744+45.8738	$0.283^{+0.003}_{-0.003}$	$-48164.7^{+254.1}_{-231.0}$	$1924.3^{+19.0}_{-17.3}$	$114.7^{+2.3}_{-2.0}$	$48.1^{+2.6}_{-2.9}$	$2.18^{+0.08}_{-0.08}$	Thick
Pristine_113.7050+45.5860	$0.183^{+0.001}_{-0.001}$	$-46030.8^{+217.4}_{-201.9}$	$2185.0^{+9.7}_{-9.3}$	$50.7^{+0.5}_{-0.5}$	$7.0^{+0.6}_{-0.5}$	$0.68^{+0.03}_{-0.03}$	Thin
Pristine_180.0750+16.3239	$0.123^{+0.001}_{-0.001}$	$-54599.6^{+163.1}_{-175.7}$	$1849.1^{+7.1}_{-6.8}$	$19.1^{+0.3}_{-0.3}$	$1.4^{+0.1}_{-0.1}$	$0.23^{+0.01}_{-0.01}$	Thin
Pristine_180.8898+15.6500	$0.884^{+0.045}_{-0.045}$	$-66554.2^{+2470.1}_{-1940.8}$	$-214.9^{+129.9}_{-146.1}$	$781.1^{+37.0}_{-33.3}$	$21.2^{+3.6}_{-3.0}$	$1.33^{+0.16}_{-0.07}$	Thick
Pristine_180.8994+16.3260	$0.159^{+0.002}_{-0.002}$	$-51835.9^{+185.6}_{-212.1}$	$1859.9^{+18.3}_{-26.8}$	$33.8^{+1.2}_{-0.9}$	$51.1^{+11.0}_{-7.5}$	$1.96^{+0.18}_{-0.17}$	Thick
Pristine_181.4437+13.4888	$0.287^{+0.016}_{-0.019}$	$-67335.9^{+588.7}_{-504.6}$	$1204.3^{+37.1}_{-37.1}$	$79.9^{+9.9}_{-9.6}$	$67.2^{+4.5}_{-3.9}$	$1.95^{+0.10}_{-0.07}$	Thick
Pristine_182.2972+13.1228	$0.804^{+0.036}_{-0.038}$	$-68685.1^{+418.6}_{-307.0}$	$436.4^{+64.1}_{-66.6}$	$588.2^{+51.3}_{-45.8}$	$37.2^{+1.8}_{-1.8}$	$1.71^{+0.05}_{-0.13}$	Thick
Pristine_183.1390+16.1839	$0.199^{+0.022}_{-0.023}$	$-65222.0^{+752.9}_{-695.0}$	$1396.1^{+40.7}_{-39.1}$	$39.3^{+8.4}_{-8.1}$	$24.2^{+2.7}_{-2.5}$	$1.02^{+0.08}_{-0.07}$	Thick
Pristine_183.4550+17.0927	$0.476^{+0.022}_{-0.036}$	$-57319.9^{+383.1}_{-383.1}$	$1263.8^{+60.6}_{-41.1}$	$262.4^{+32.5}_{-41.8}$	$80.6^{+7.4}_{-9.6}$	$2.59^{+0.14}_{-0.25}$	Thick
Pristine_185.5596+15.5893	$0.405^{+0.020}_{-0.020}$	$-47302.1^{+716.9}_{-665.7}$	$1830.2^{+4.5}_{-4.7}$	$241.0^{+29.3}_{-26.2}$	$25.1^{+0.8}_{-0.7}$	$1.66^{+0.09}_{-0.07}$	Thick
Pristine_188.4543+15.1750	$0.146^{+0.005}_{-0.004}$	$-54018.1^{+90.2}_{-90.2}$	$1843.8^{+7.0}_{-6.7}$	$27.2^{+1.8}_{-1.6}$	$9.5^{+0.6}_{-0.6}$	$0.69^{+0.02}_{-0.02}$	Thin
Pristine_191.9208+16.0031	$0.305^{+0.160}_{-0.093}$	$-65487.5^{+1531.9}_{-1276.6}$	$1083.7^{+184.8}_{-261.7}$	$83.1^{+89.6}_{-44.8}$	$172.5^{+61.6}_{-46.2}$	$3.56^{+1.13}_{-0.71}$	Thick
Pristine_192.4508+12.7922	$0.297^{+0.016}_{-0.016}$	$-60309.6^{+161.1}_{-115.1}$	$1495.4^{+20.5}_{-21.2}$	$97.6^{+10.5}_{-9.4}$	$15.6^{+1.2}_{-1.2}$	$0.91^{+0.04}_{-0.04}$	Thin
Pristine_193.5777+10.3945	$0.649^{+0.058}_{-0.025}$	$-70002.9^{+92.0}_{-73.6}$	$523.3^{+50.8}_{-54.7}$	$392.5^{+27.5}_{-24.5}$	$163.8^{+8.8}_{-8.8}$	$4.28^{+0.25}_{-0.21}$	Halo
Pristine_195.1494+06.5655	$0.748^{+0.017}_{-0.018}$	$-13651.5^{+1986.9}_{-1821.3}$	$41.1^{+98.7}_{-94.6}$	$1864.6^{+203.6}_{-162.9}$	$2153.3^{+52.0}_{-55.9}$	$38.35^{+2.64}_{-2.15}$	Halo
Pristine_198.3167+14.9688	$0.123^{+0.002}_{-0.002}$	$-57589.0^{+242.5}_{-223.9}$	$1715.0^{+11.5}_{-9.8}$	$17.8^{+0.7}_{-0.6}$	$10.2^{+0.5}_{-0.6}$	$0.65^{+0.02}_{-0.02}$	Thin
Pristine_206.8050+00.7423	$0.688^{+0.066}_{-0.100}$	$-74524.1^{+1009.5}_{-415.7}$	$584.7^{+165.2}_{-130.8}$	$383.3^{+67.7}_{-74.5}$	$31.1^{+5.7}_{-5.5}$	$1.32^{+0.19}_{-0.16}$	Thick
Pristine_206.9304+11.8894	$0.932^{+0.020}_{-0.027}$	$-68746.9^{+735.4}_{-686.4}$	$-46.2^{+66.0}_{-61.6}$	$838.6^{+12.0}_{-14.8}$	$10.2^{+0.2}_{-0.2}$	$1.03^{+0.02}_{-0.01}$	Thick
Pristine_212.2541+11.4580	$0.871^{+0.059}_{-0.189}$	$-55237.6^{+62464.4}_{-1.0}$	$52.8^{+440.9}_{-440.9}$	$126.6^{+1.0}_{-1.0}$	$447.6^{+1290.5}_{-1.0}$	$14.19^{+101.54}_{-6.77}$	Halo
Pristine_213.1910+14.7927	$0.583^{+0.029}_{-0.086}$	$-56836.4^{+17888.5}_{-5962.8}$	$497.0^{+265.9}_{-422.4}$	$129.7^{+1.0}_{-1.0}$	$648.8^{+1019.1}_{-291.2}$	$9.07^{+7.84}_{-3.14}$	Halo
Pristine_216.1506+14.1298	$0.877^{+0.059}_{-0.029}$	$-26807.1^{+59580.8}_{-14895.2}$	$-475.8^{+341.4}_{-443.8}$	$796.4^{+1.0}_{-1.0}$	$734.5^{+1047.6}_{-349.2}$	$22.94^{+19.59}_{-11.76}$	Halo
Pristine_219.0145+11.6057	$0.298^{+0.011}_{-0.012}$	$-46200.0^{+476.3}_{-408.3}$	$2017.7^{+2.1}_{-2.1}$	$133.8^{+11.4}_{-11.0}$	$36.4^{+5.0}_{-5.0}$	$1.99^{+0.18}_{-0.19}$	Thick
Pristine_232.8856+07.8678	$0.274^{+0.030}_{-0.020}$	$-70980.0^{+939.9}_{-1110.8}$	$1131.5^{+44.1}_{-50.2}$	$67.4^{+11.2}_{-8.6}$	$55.2^{+2.9}_{-2.7}$	$1.62^{+0.06}_{-0.05}$	Thick
Pristine_234.0338+12.6370	$0.400^{+0.011}_{-0.009}$	$-65861.8^{+515.2}_{-554.8}$	$994.1^{+25.1}_{-25.1}$	$157.9^{+5.5}_{-4.7}$	$173.8^{+1.5}_{-1.3}$	$3.84^{+0.03}_{-0.03}$	Thick
Pristine_235.0278+07.5059	$0.388^{+0.047}_{-0.047}$	$-77380.5^{+909.0}_{-530.3}$	$481.1^{+103.1}_{-91.6}$	$74.6^{+13.1}_{-12.4}$	$397.7^{+53.8}_{-47.4}$	$4.74^{+0.63}_{-0.24}$	Halo
Pristine_235.0537+07.5988	$0.746^{+0.039}_{-0.053}$	$-78390.9^{+670.8}_{-545.0}$	$-468.7^{+70.4}_{-81.2}$	$434.6^{+35.8}_{-38.5}$	$7.5^{+0.5}_{-0.3}$	$0.55^{+0.02}_{-0.01}$	Thick
Pristine_236.4719+15.3328	$0.871^{+0.029}_{-0.097}$	$-73351.7^{+330.4}_{-220.3}$	$185.0^{+70.4}_{-67.7}$	$674.3^{+38.7}_{-38.7}$	$12.8^{+3.0}_{-2.3}$	$0.96^{+0.09}_{-0.02}$	Thin
Pristine_236.7635+05.4474	$0.773^{+0.026}_{-0.026}$	$-57119.4^{+117.0}_{-117.0}$	$625.8^{+71.8}_{-68.6}$	$699.9^{+45.7}_{-41.8}$	$68.3^{+2.8}_{-1.7}$	$3.09^{+0.12}_{-0.06}$	Thick
Pristine_237.8581+07.1456	$0.761^{+0.027}_{-0.035}$	$-49125.4^{+4286.9}_{-3980.7}$	$314.7^{+91.0}_{-84.5}$	$742.8^{+159.8}_{-125.6}$	$581.8^{+78.3}_{-69.9}$	$13.68^{+2.55}_{-2.38}$	Halo
Pristine_238.2716+07.5917	$0.560^{+0.041}_{-0.053}$	$-80881.5^{+1320.5}_{-1100.4}$	$550.6^{+90.5}_{-95.5}$	$194.5^{+22.9}_{-20.5}$	$132.1^{+19.5}_{-18.4}$	$2.84^{+0.30}_{-0.26}$	Thick
Pristine_240.2908+07.9401	$0.655^{+0.077}_{-0.073}$	$-53144.1^{+3606.9}_{-2705.2}$	$740.5^{+138.5}_{-147.7}$	$509.7^{+167.7}_{-115.3}$	$329.7^{+58.4}_{-49.4}$	$8.43^{+0.80}_{-1.59}$	Halo
Pristine_241.1299+06.3632	$0.579^{+0.021}_{-0.027}$	$-72550.9^{+1145.0}_{-1049.6}$	$757.8^{+58.1}_{-55.7}$	$285.4^{+17.6}_{-16.9}$	$59.2^{+1.4}_{-1.3}$	$1.94^{+0.08}_{-0.04}$	Thick
Pristine_246.4406+15.0900	$0.774^{+0.038}_{-0.031}$	$-39353.9^{+4164.6}_{-3239.1}$	$943.5^{+58.8}_{-52.6}$	$1062.0^{+210.5}_{-161.0}$	$126.4^{+22.9}_{-17.8}$	$6.68^{+1.71}_{-1.14}$	Halo

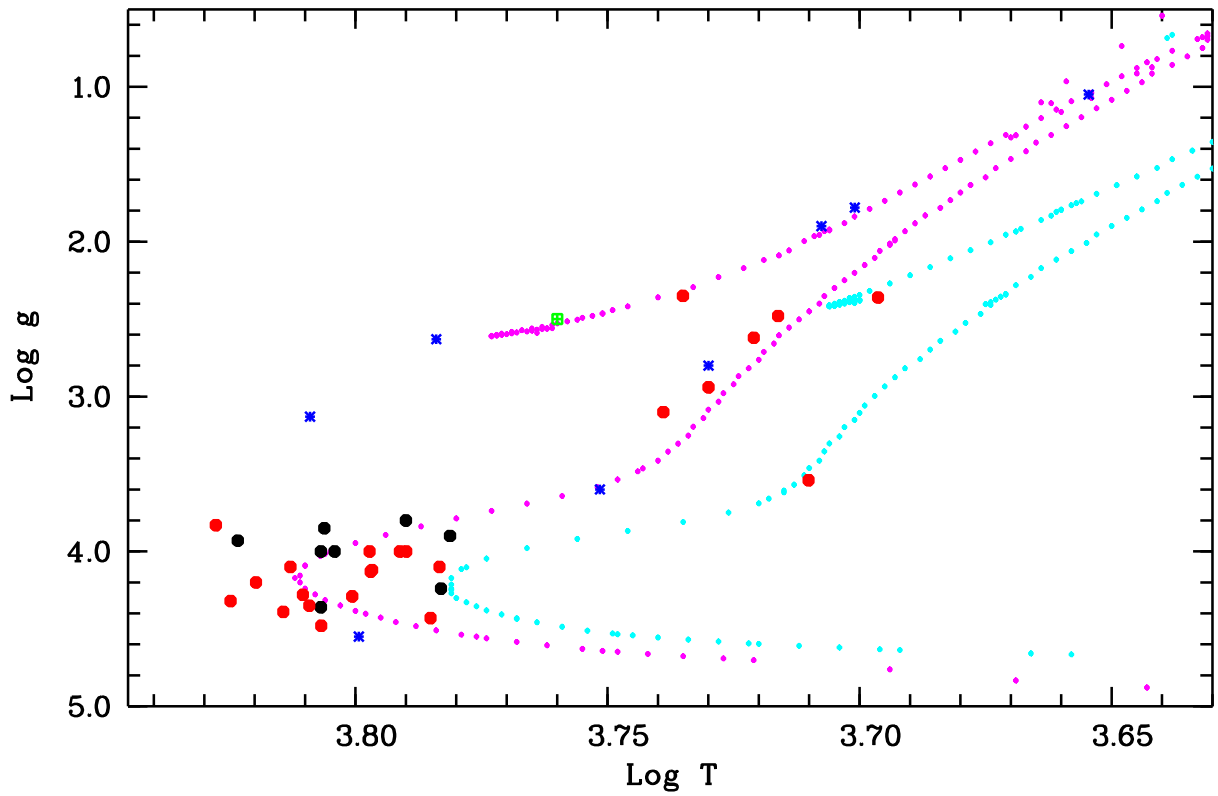

Figure B1. The log ($T_{\rm eff}$) - log g diagram for our stars. Black dots are stars classified as "Thin", red dots are stars classified as "Thick" and blue asterisks are stars classified as "Halo", the green crossed square is the star Pristine_216.1506+14.1298. The cyan dots are a PARSEC isochrone of 11.5 Gyr and metallicity −0.5 and the magenta dots one of metallicity −1.5.

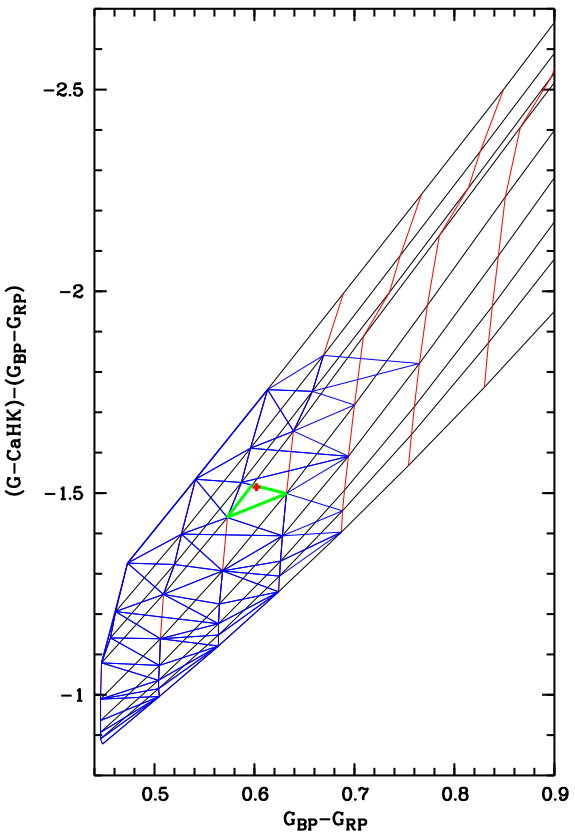

Figure C1. Illustration of how the triangle for interpolation is detemined. The underlying grid is the theoreticla colours interpolated for log g = 3.84 (black lines of constant metallicity, red of constant effective temperature), in blue a part of the Delaunay triangulation and in green the refined triangle (non-Delaunay) that is used to estimate the final metallicity. The red cross corresponds to the observed colours.